An extension of the second moment closure model for turbulent flows over macro rough walls

An extension of the second moment closure model for turbulent flows over macro rough walls

Y. Kuwata[a,*], K. Suga[a], Y. Kawaguchi[b]

[a]*Department of Mechanical Engineering, Osaka Prefecture University, Sakai, Osaka 599-8531, Japan*
[b]*Department of Mechanical Engineering, Tokyo University of Science, 2641 Yamazaki, Noda, Chiba 278-8510, Japan*

Abstract

An advanced second moment closure for rough wall turbulence is proposed. In contrast to previously proposed models relying on an empirical correlation based on equivalent sand grain roughness, the proposed model mathematically derives roughness effects by applying spatial and Reynolds averaging to the governing equations. The additional terms in the momentum equations are the drag force and inhomogeneous roughness density terms. The drag force term is modeled with respect to the plane porosity and plane hydraulic diameter. The two-component limit pressure-strain model is applied to the additional pressure-strain term, which is related to the external force terms. An evaluation of turbulence over surfaces with randomly distributed semi-spheres confirms that the developed model reasonably reproduces the effects of roughness on mean velocity, Reynolds stress, and energy dissipation. Turbulence over rough surfaces of marine paint is also simulated to assess the predictive performance for higher Reynolds number turbulent flows over real rough surfaces. The developed model successfully reproduces the dependence of the Reynolds number on roughness effects. Moreover, qualitative agree-

*corresponding author
Email address: kuwata@me.osakafu-u.ac.jp (Y. Kuwata)

ment of the skin friction increase with the experimental data is confirmed.

Keywords: Turbulence modeling, Rough wall turbulence, Double averaging, Second moment closure

1. Introduction

Predicting fluid flow over rough surfaces is an important prerequisite for engineering design because wall surfaces encountered in engineering flows are usually rough. The wall roughness inevitably occurs in production processes due to imperfections in the surface finish. Furthermore, erosion or corrosion due to aging and fouling processes also roughen surfaces; e.g., aerodynamic flows over airfoils with icing (Dalili et al., 2009; Parent and Ilinca, 2011), ship hull roughness due to organic fouling (Townsin, 2003; Schultz, 2007), or erosion of turbine blades by impinging combustor air (Bons, 2010). It is well known that those rough surfaces lead to performance degradation due to a significant increase in wall-friction.

The most important effect of wall roughness on turbulent flow is a downward shift in the mean velocity profile, known as the roughness function due to a modified friction factor (Hama, 1954; Schlichting et al., 1960). The pioneering experimental work on this effect was performed by Nikuradse (1933). His large number of measurements of pressure drop in pipes with walls covered by sand grains revealed that the friction factor only depends on the sand grain roughness scale at sufficiently high Reynolds numbers. Colebrook et al. (1939) extended this work by including the data in transitionally-rough turbulent flow for more practical uses. Moody (1944) later consolidated the data as a Moody diagram, which is the most widely used engineering tool for estimating the friction factor. Because the diagram was based on the equivalent roughness, many studies have dedicated their efforts to determining the equivalent sand grain roughness from topological roughness parameters (e.g., Schlichting et al., 1960; Dvorak, 1969; Dirling, 1973; Musker, 1980; Sigal and Danberg, 1990; Flack and Schultz, 2010; Forooghi et al., 2017; Kuwata and Kawaguchi, 2018b). These were based on the roughness density and shape parameter (Dirling, 1973; Sigal and Danberg, 1990; Van Rij et al., 2002), or statistical moments of the roughness height elevation (Musker, 1980; Townsin et al., 1981; Flack and Schultz, 2010; Kuwata and Kawaguchi, 2018b). Another important strategy, which was originally not intended for the equivalent roughness but the roughness function, is based on the slope of a roughness corrugation (Napoli et al., 2008; Schultz and Flack, 2009; Forooghi et al., 2017; Chan et al., 2015). Indeed, those correlations were used to successfully estimate an increase in the rough wall skin friction. However, one can readily expect that those correlations cannot be used to predict wall roughness effects in practical flow problems where flow separation, reattachment, and impingement sometimes occur due to complex wall geometries. Accordingly, in order to predict the impact of roughness on such engineering flows with relatively low computational cost many studies attempted to extend the Reynolds-Averaged-Navier–Stokes (RANS) turbulence model to account for the roughness effects (Christoph and Pletcher, 1983; Taylor et al., 1985; Patel and Yoon, 1995; Wilcox et al., 1998; Durbin et al., 2001; Aupoix and Spalart, 2003; Suga et al., 2006; Knopp et al., 2009; Qi et al., 2018).

An early attempt at modeling roughness effects was made by Taylor et al. (1985); he modeled the blockage and drag force effects due to the presence of roughness. Validation in flows over surfaces with two-dimensional roughness demonstrated that the roughness model in conjunction with the mixing length model could be used to successfully predict the dependence of skin friction on rib spacing, rib size, and Reynolds number, although the application examples were limited to surfaces with simple roughness elements. Roughness modification with the widely-used, robust two-equation $k-\omega$ SST model was reported by Wilcox et al. (1998). He modified only the wall boundary condition of ω using the equivalent roughness. In spite of a very simple modification, the developed model could be used to reasonably predict the decreased mean velocity over rough surfaces. However, Patel and Yoon (1995); Hellsten (1997); Knopp et al. (2009) pointed out a major drawback of the modification presented by Wilcox et al. (1998) in that the model required very fine near-wall mesh resolution. Durbin et al. (2001) also extended the two-layer $k-\varepsilon$ model. They modified the eddy viscosity in the vicinity of a rough wall by introducing the equivalent roughness and imposed non-zero turbulence energy at the rough wall boundary. Their modifications relied on a log-law profile over a surface with sand grain roughness of Nikuradse (1933). Similar modifications based on the log-law solution were also reported by Aupoix and Spalart (2003); Knopp et al. (2009). Flows past an airfoil were simulated for a variety of angle of attack using the extended $k-\omega$ model Knopp et al. (2009) where an adverse pressure gradient presented. They demonstrated the potential of predicting the effects of roughness on the lift coefficient; however, the simulated results did not quantitatively agree with the experimental data. Using a similar idea to those of Durbin et al. (2001); Aupoix and Spalart (2003); Knopp et al. (2009), Suga et al. (2006) extended the analytical wall function developed by the UMIST group (Craft et al., 2004) to account for the effects of fine-grain surface roughness. They modified the viscous sublayer thickness by using the equivalent roughness in order to mimic how roughness disrupts the viscous sublayer. They predicted sufficient results for flows over curved rough walls, sand dunes, and a roughed ramp, as well as boundary layer flows over a rough-wall.

Those turbulence models showed good performance in predicting turbulent flow over rough surfaces. However, those models basically relied on an equivalent roughness; thus, their application is limited to rough surfaces whose equivalent roughness is known a priori. Applicable examples include commercial steel pipes, glass, and concrete, while applying those to naturally occurring roughness with unknown equivalent roughness is not straightforward (e.g., roughness by corrosion, erosion, icing, or organic fouling). Another concern of those models is that they describe transitionally-rough turbulence based on empirical asymptotic correlations for sand grain roughness (Nikuradse, 1933) or hemispheres roughness (Ligrani and Moffat, 1986), despite the fact that there is no universal correlation between the equivalent roughness and roughness function in this regime (Jiménez, 2004; Flack et al., 2012; Thakkar et al., 2017). Therefore, those models may not provide a reasonable prediction of turbulence over a variety of rough surfaces in the transitionally rough regime.

A different approach for simulating rough wall turbulence has been discussed in terms of direct numerical simulation (DNS)(Miyake et al., 2000; Busse and Sandham, 2012; Forooghi et al., 2018a; Kuwata and Kawaguchi, 2018a). Their simulations were basically DNS, but an external drag force term was introduced to account for the blocking effects due to the rough wall. Hence, empirical correlation based on the equivalent roughness is not used in those models. Recently, Forooghi et al. (2018a); Kuwata and Kawaguchi (2018a) compared the model simulation results with those obtained by DNS of turbulence over fully-resolved rough surfaces, and they showed almost perfect agreement of the standard turbulence statistics with the DNS data. In addition, Kuwata and Kawaguchi (2018a) confirmed that the modified turbulence structure and transport due to the wall roughness were correctly reproduced by their model, where the additional roughness terms were mathematically derived by applying spatial (plane) averaging theory. However, it should be stressed again that the computational cost is too huge for practical applications because those models do not include a turbulence model.

Following this strategy, the aim of the present study is to develop a more elaborate turbulence model starting from the plane averaged Navier–Stokes (PANS) model of Kuwata and Kawaguchi (2018a), which was rigorously validated through a comparison with DNS data. By applying Reynolds averaging in addition to the plane averaging, we attempt a first step towards establishing a second moment closure for rough wall turbulence based on the most advanced SMC model, namely the TCL (two-component limit) model of (Craft and Launder, 1996). Unlike a previous phenomenological strategy that relies on the equivalent roughness, the present study faithfully treats the mathematically derived additional terms representing roughness effects. The developed model is first validated in transitionally-rough turbulence over surfaces with semi-spheres. The turbulence statistics, including mean velocity, Reynolds stress, energy dissipation rate, and drag force terms, are evaluated against the DNS and PANS results of Kuwata and Kawaguchi (2018a). A second validation is performed for fully-rough turbulence over rough surfaces with marine paint. In order to assess the predictive performance for higher Reynolds number turbulent flows over real rough surfaces.

Nomenclature

A_S : plane area of a representative elementary plane

A_{S_f} : plane area of fluid phase contained within a representative elementary plane

C_f : Skin friction coefficient

C_1^D, C_2^D : model coefficients of the plane-averaged drag force model

D_m : plane hydraulic diameter

ES : effective slope

f_i : plane-averaged drag force

g_i^φ : inhomogeneous roughness density term

h_m : mean roughness height

h_{max} : maximum peak height of a rough surface

h_{rms} : standard deviation of roughness elevation

H : channel height

k : turbulence energy: $k = R_{kk}/2$

ℓ : circumference length of solid obstacles

p : pressure

R_{ij} : Reynolds stress: $\overline{\langle u_i' \rangle^f \langle u_j' \rangle^f}$

Re_τ : friction Reynolds number: $Re_\tau = u_\tau \delta/\nu$

Re_b : bulk mean Reynolds number: $Re_b = U_b H/\nu$

Sk : skewness of roughness elevation

t : time

u_i : velocity

u_τ : friction velocity

U_b : bulk mean velocity

x : streamwise coordinate

y : wall-normal coordinate

z : spanwise coordinate

δ_{ij} : Kronecker delta

δ : boundary layer thickness

ΔU : roughness function

ε : isotropic part of the energy dissipation rate

ν : kinematic viscosity

τ_{ij} : dispersive stress: $\tau_{ij} = \varphi \langle \tilde{u}_i \tilde{u}_j \rangle^f$

ρ : fluid density

φ : plane porosity: $\varphi = A_{S_f}/A_s$

ϕ : variable

$\overline{\phi}$: Reynolds averaged value of ϕ

ϕ' : temporal fluctuation of ϕ : $\phi - \overline{\phi}$

$\langle\phi\rangle^f$: intrinsic plane-averaged value of ϕ

$\langle\phi\rangle$: superficial plane-averaged value of ϕ

$()^+$: values normalized by the friction velocity

2. Spatial averaged Navier–Stokes equation

Before we discuss an extension of the base PANS model of Kuwata and Kawaguchi (2018a), we briefly describe spatial (plane) averaging theory. The present study applies plane averaging to the governing equations in order to macroscopically describe fluid flow near a rough wall. To account for the nature of rough surfaces whose characteristics vary drastically depending on the rough wall-normal coordinate, we define a representative elementary plane (REP) for spatial averaging that is parallel to the rough wall, as illustrated in Fig.1. The typical size of the REP can be defined such that the average roughness parameters over the REP are independent of the plane size, but it should be smaller than the global flow geometry (see Kuwata and Kawaguchi (2018a) for the discussions on the REP size). The superficial plane average of the flow velocity u_i is

$$\langle u_i\rangle = \frac{1}{A_S}\int_S u_i dS, \quad (1)$$

where S and A_S are the REP and its plane area, respectively. As flow within rough surface is spatially inhomogeneous, the velocity u_i can be decomposed into a contribution from the intrinsic (fluid phase) averaged value $\langle u_i \rangle^f$:

$$\langle u_i \rangle^f = \frac{1}{A_{S_f}} \int_S u_i dS, \tag{2}$$

and a deviation from the intrinsic (fluid phase) averaged value $\tilde{u}_i$, which is usually referred to as the dispersion:

$$u_i = \langle u_i \rangle^f + \tilde{u}_i, \tag{3}$$

where A_{S_f} denotes the plane area of the fluid phase contained within S and there is a relation between the superficial and intrinsic plane-averaged values: $\langle u_i \rangle = \varphi \langle u_i \rangle^f$. Here, the plane porosity φ is defined as the ratio of the fluid phase plane area A_{S_f} to the plane area A_S: $\varphi = A_{S_f}/A_S$. Plane averaging can be applied to the momentum equations for incompressible flows, yielding the plane averaged Navier–Stokes (PANS) equation (Kuwata and Kawaguchi, 2018a):

$$\begin{aligned}
\frac{\partial \langle u_i \rangle^f}{\partial t} + \langle u_j \rangle^f \frac{\partial \langle u_i \rangle^f}{\partial x_j} &= -\frac{1}{\rho}\frac{\partial \langle p \rangle^f}{\partial x_i} + \frac{1}{\varphi}\frac{\partial}{\partial x_j}\left(\nu \frac{\partial \varphi \langle u_i \rangle^f}{\partial x_j}\right) \\
&\quad -\frac{1}{\varphi}\frac{\partial}{\partial x_j}\underbrace{\varphi \langle \tilde{u}_i \tilde{u}_j \rangle^f}_{\tau_{ij}} \underbrace{-\frac{\nu}{\varphi}\frac{\partial \varphi}{\partial x_j}\frac{\partial \langle u_i \rangle^f}{\partial x_j}}_{g_i^{\varphi}} \\
&\quad -\underbrace{\left(\frac{1}{\rho A_{S_f}}\int_L \tilde{p} n_i d\ell - \frac{\nu}{A_{S_f}}\int_L n_k \frac{\partial \tilde{u}_i}{\partial x_k} d\ell\right)}_{f_i},
\end{aligned} \tag{4}$$

where L represents obstacle perimeter within the REP, ℓ is the circumference length of solid obstacles, and n_k is its unit normal vector pointing outward from the fluid to the solid phase. The spatial averaging process produces an additional stress term τ_{ij}, called dispersive stress, which consists of velocity dispersion $\tilde{\boldsymbol{u}}$ (Raupach and Shaw, 1982). This also yields an inhomogeneous roughness density term g_i^φ and a plane-averaged drag force term f_i. The plane-averaged drag force is expressed as a line integral of the dispersive viscous stress and dispersive pressure, representing the viscous and foam drag effects, respectively. The term g_i^φ does not require any approximation, whereas the term τ_{ij} and f_i must be modeled to close Eq.(4). In our previous work, Kuwata and Kawaguchi (2018a) modeled f_i by using two geometric roughness parameters, namely the plane porosity φ and plane hydraulic diameter D_m as

$$f_i = \nu C_1^D \langle u_i \rangle^f + C_2^D \langle u_i \rangle^f \sqrt{\langle u_k \rangle^f \langle u_k \rangle^f}, \tag{5}$$

where the model coefficients C_1^D and C_2^D were modeled in terms of D_m and φ as follows:

$$C_1^D = \frac{2C_1}{\pi} \frac{(1-\varphi)}{\varphi^2 D_m^2}, \qquad C_2^D = \frac{2C_2}{\pi} \frac{(1-\varphi)}{\varphi^{2.5} D_m}, \tag{6}$$

where the model constants were $C_1 = 71$ and $C_2 = 0.79$. Here, the plane hydraulic diameter D_m is the representative cross-sectional area of the roughness elements, which is defined as follows:

$$D_m = \frac{4S_{sum}}{L_{sum}}, \tag{7}$$

where S_{sum} and L_{sum} stand for the total area occupied by the obstacles and the total wetted perimeter of the obstacles in the REP, respectively. Kuwata and Kawaguchi (2018a) conducted DNS of turbulent flows over macro rough walls by solving the PANS equation (Eq.(4)) in a rough wall region in order to validate the PANS approach. They used the plane-averaged drag force model (Eq.(5)) while they dropped the dispersive stress τ_{ij}, and confirmed that the standard turbulence statistics were in almost perfect agreement with those obtained from fully resolved rough wall simulations. Furthermore, they confirmed the validity of omitting τ_{ij} and the drag force model by analyzing the budget terms in the turbulent kinetic energy transport equation. Accordingly, in the subsequent section, we attempt to extend the PANS model using the drag force model of Eq.(5). It should be noted that ignoring the dispersive stress means that the turbulence generation induced by wake flows (i.e., wake production (Raupach and Shaw, 1982)) is not taken into account in the present model. However, results from the fully-resolved roughness DNS studies in the fully-rough regime (Yuan and Piomelli, 2014; Kuwata and Kawaguchi, 2018b; Yuan and Jouybari, 2018) suggest that the majority of the turbulence generation in the roughness sublayer was occupied by the shear production rather than the wake production. Interestingly, the experimental study by Mignot et al. (2009) on higher Reynolds number flows in gravel beds, where the inner-scaled equivalent roughness exceeded 580, reached the same conclusion. Moreover, the success of the macro rough wall simulations (Busse and Sandham, 2012; Forooghi et al., 2018a; Kuwata and Kawaguchi, 2018a), in which the dispersive stress was neglected, indicates the minor contribution of the wake production in turbulence generation. However, one must keep in mind that the turbulence predicted deep inside a modeled rough wall may deviate considerably from the real turbulence because velocity dispersion cannot be neglected relative to the spatially-averaged velocity in the region.

3. Spatial and Reynolds averaged Navier–Stokes equation

The merit of the PANS simulation is that we do not have to treat complicated rough geometries. However, the PANS simulation treats time-dependent flow and uses fine grids to resolve fine-scale turbulent eddies because no turbulence model is used in the PANS simulation. Hence, the PANS simulations are likely beyond the capability of modern supercomputers when we consider engineering or environmental flows. Accordingly, to reduce computational costs, we incorporate a turbulence model in the PANS method. On that account, Reynolds averaging is used in addition to spatial averaging:

$$u_i = \overline{u_i} + u_i', \tag{8}$$

where $\overline{u_i}$ is the Reynolds-averaged velocity, and u_i' denotes the fluctuation from the averaged velocity. Applying Reynolds averaging to the PANS equation in Eq.(4) yields the spatial and Reynolds (double) averaged Navier–Stokes equation in the following form:

$$\begin{aligned}\frac{\partial \langle \overline{u}_i \rangle^f}{\partial t} + \langle \overline{u}_j \rangle^f \frac{\partial \langle \overline{u}_i \rangle^f}{\partial x_j} &= -\frac{1}{\rho}\frac{\partial \langle \overline{p} \rangle^f}{\partial x_i} + \frac{1}{\varphi}\frac{\partial}{\partial x_j}\left(\nu \frac{\partial \varphi \langle \overline{u}_i \rangle^f}{\partial x_j}\right) \\ &\quad -\frac{1}{\varphi}\frac{\partial}{\partial x_j}\varphi \underbrace{\overline{\langle u_i' \rangle^f \langle u_i' \rangle^f}}_{R_{ij}} + \overline{g}_i^{\varphi} - \overline{f}_i \end{aligned} \tag{9}$$

where R_{ij} is the plane-averaged Reynolds stress. Here, the correlation terms related to the dispersive stress τ_{ij} are all neglected (see Kuwata and Suga (2015) in the exact form of the double averaged Navier–Stokes (DANS) equation). Reynolds averaging is applied to the spatially-averaged equation in the present study. However, one should note that the order of the spatial and Reynolds averaging operators is interchangeable, and the resulting forms are mathematically equivalent (Pedras and de Lemos, 2001).

Reynolds averaging of the plane-averaged drag force term can be expressed as

$$\overline{f}_i = \nu C_1^D \langle \overline{u_i} \rangle^f + C_2^D \overline{\langle u_i \rangle^f \sqrt{\langle u_k \rangle^f \langle u_k \rangle^f}}, \tag{10}$$

The modelled form of Eq.(5) consists of linear and quadratic terms with respect to the fluid velocity, and this form is the same as the Forchheimer-extended Darcy model, which is widely used to model flow resistance due to porous media (Whitaker, 1996). Because the quadratic term cannot be strictly treated, the Reynolds-averaged Darcy-Forchheimer model is usually modelled as a simple form (Chan et al., 2007; Silva and de Lemos, 2003) with the assumption that

$$\overline{\sqrt{\langle u_k \rangle^f \langle u_k \rangle^f}} \approx \sqrt{\langle \overline{u}_k \rangle^f \langle \overline{u}_k \rangle^f}. \tag{11}$$

This assumption yields

$$\overline{f}_i = \nu C_1^D \langle \overline{u_i} \rangle^f + C_2^D \langle \overline{u_i} \rangle^f \sqrt{\langle \overline{u}_k \rangle^f \langle \overline{u}_k \rangle^f} \tag{12}$$

The assumption in Eq.(11) may be valid for relatively low Reynolds number flows in porous media, where the contribution from the turbulent velocity fluctuation is sufficiently smaller than that from the mean velocity. However, one can expect that the turbulent velocity fluctuation remains significant just below the roughness crest and the assumption cannot be applicable in this region. Accordingly, in order to account for the influence of velocity fluctuations on the squared velocity $\langle u_k \rangle^f \langle u_k \rangle^f$, we choose the more sophisticated model proposed by Getachew et al. (2000). They assumed that $\left(\langle \bar{u}_k \rangle^f\right)^2 >> \left(\langle u'_k \rangle^f\right)^2$ and applied the binomial series expansion to

$\left\{\left(\langle\bar{u}_k\rangle^f\right)^2 + 2\langle\bar{u}_k\rangle^f\langle u'_k\rangle^f\right\}^{1/2}$, yielding

$$\left\{\left(\langle\bar{u}_k\rangle^f\right)^2\right\}^{1/2}\left[1+\frac{\langle\bar{u}_l\rangle^f\langle u'_l\rangle^f}{\left(\langle\bar{u}_m\rangle^f\right)^2}-\frac{1}{2}\left\{\frac{\langle\bar{u}_l\rangle^f\langle u'_l\rangle^f}{\left(\langle\bar{u}_m\rangle^f\right)^2}\right\}^2+\frac{1}{2}\left\{\frac{\langle\bar{u}_l\rangle^f\langle u'_l\rangle^f}{\left(\langle\bar{u}_m\rangle^f\right)^2}\right\}^3\cdots\right], \tag{13}$$

and we can expand the double averaged drag force term as follows:

$$\overline{f}_i = \nu C_1^D\langle\overline{u}_i\rangle^f + C_2^D\langle\overline{u}_i\rangle^f\sqrt{\langle\overline{u}_k\rangle^f\langle\overline{u}_k\rangle^f} + C_2^D\frac{\langle\overline{u}_k\rangle^f}{\sqrt{\langle\overline{u}_l\rangle^f\langle\overline{u}_l\rangle^f}}R_{ik}. \tag{14}$$

In addition to the second term on the right-hand side of Eq.(12), which represents the contribution from the mean velocity, the binomial expansion generates an additional higher-order term (the third term on the right-hand side of Eq.(14)) that models the effect of velocity fluctuations on the quadratic term. One may suppose that faithfully averaging the form may be worthless because the plane-averaged drag force in Eq.(5) is just a model. However, Forooghi et al. (2018a) conducted DNS of turbulence over a macro-rough wall and solved the spatially-averaged equations with the similar drag force model; the results show that the simple model of Eq.(12) substantially underpredicts as it does not account for velocity fluctuations (the contribution from the higher order term will be discussed in detail in §4.1.4).

In contrast to $\overline{f}_i$, the Reynolds-averaged form $\overline{g}_i^\varphi$ straightforwardly written as follows:

$$\overline{g}_i^\varphi = -\frac{\nu}{\varphi}\frac{\partial\varphi}{\partial x_j}\frac{\partial\langle\overline{u}_i\rangle^f}{\partial x_j}, \tag{15}$$

where $\overline{g}_i^\varphi$ does not require an approximation.

3.1. Modeling the Reynolds stress transport equation

A second moment closure route was chosen to elaborately model the Reynolds stress in this study because this route can directly account for the effects of roughness on the Reynolds stress components. The transport equation of R_{ij} may be written as

$$\frac{\partial R_{ij}}{\partial t} + \langle \overline{u_k} \rangle^f \frac{\partial R_{ij}}{\partial x_k} = \mathcal{D}_{ij} + \Pi_{ij} + P_{ij} + F_{ij} + G^{\varphi}_{ij} - \varepsilon_{ij}, \tag{16}$$

where

$$\mathcal{D}_{ij} = \underbrace{\frac{\partial}{\partial x_k}\left(\nu \frac{\partial R_{ij}}{\partial x_k}\right)}_{\mathcal{D}^{\nu}_{ij}} \underbrace{- \frac{1}{\varphi}\frac{\partial}{\partial x_k}\left(\varphi \overline{\langle u'_i \rangle^f \langle u'_j \rangle^f \langle u'_k \rangle^f}\right)}_{\mathcal{D}^{t}_{ij}}, \tag{17}$$

$$\Pi_{ij} = -\frac{1}{\rho}\left(\overline{\langle u'_j \rangle^f \frac{\partial \langle p' \rangle^f}{\partial x_i}} + \overline{\langle u'_i \rangle^f \frac{\partial \langle p' \rangle^f}{\partial x_j}}\right), \tag{18}$$

$$P_{ij} = -R_{ik}\frac{\partial \langle \bar{u}_j \rangle^f}{\partial x_k} - R_{jk}\frac{\partial \langle \bar{u}_i \rangle^f}{\partial x_k}, \tag{19}$$

$$\varepsilon_{ij} = 2\nu \overline{\frac{\partial \langle u'_i \rangle^f}{\partial x_k}\frac{\partial \langle u'_j \rangle^f}{\partial x_k}}. \tag{20}$$

The terms $\mathcal{D}^{\nu}_{ij}$, $\mathcal{D}^{t}_{ij}$, Π_{ij}, P_{ij}, and ε_{ij} are the molecular diffusion, turbulent diffusion, pressure-correlation, mean shear production, and dissipation rate terms, respectively. The additional source terms due to roughness are the drag force contribution term $F_{ij} = \overline{f_i \langle u'_j \rangle^f} + \overline{f_j \langle u'_i \rangle^f}$ and the inhomogeneous roughness density term $G^{\varphi}_{ij} = \overline{g^{\varphi}_i \langle u'_j \rangle^f} + \overline{g^{\varphi}_j \langle u'_i \rangle^f}$, which are respectively written as

$$
\begin{aligned}
F_{ij} &= -2\nu C_1^D R_{ij} \\
&\quad -\frac{C_2^D \langle \overline{u}_k \rangle^f}{\sqrt{\langle \overline{u}_m \rangle^f \langle \overline{u}_m \rangle^f}} \left(2\langle \overline{u}_k \rangle^f R_{ij} + \langle \overline{u}_i \rangle^f R_{jk} + \langle \overline{u}_j \rangle^f R_{ik} - c_s \tau R_{kl} \frac{\partial R_{ij}}{\partial x_l} \right). \\
G_{ij}^{\varphi} &= \frac{\nu}{\varphi} \left(2R_{ij} \frac{\partial^2 \varphi}{\partial x_k^2} + \frac{\partial R_{ij}}{\partial x_k} \frac{\partial \varphi}{\partial x_k} \right), \qquad (21)
\end{aligned}
$$

Note that G_{ij}^{φ} can be treated in an exact manner in the second moment closure because R_{ij} is given by solving its transport equation, whereas the binomial expansion is used to derive F_{ij}, as in Getachew et al. (2000). The present model adopts the usual generalized gradient diffusion hypothesis (GGDH) of Daly and Harlow (1970) to model the triple velocity correlations in $\mathcal{D}_{ij}^t$:

$$
\mathcal{D}_{ij}^t = \frac{1}{\varphi} \frac{\partial}{\partial x_k} \left\{ \varphi \left(c_s \tau R_{kl} \right) \frac{\partial R_{ij}}{\partial x_l} \right\}, \qquad (22)
$$

where τ is the turbulent time scale $\tau = k/\varepsilon$, and the model constant is $c_s = 0.22$. Here, the turbulent kinetic energy is $k = R_{kk}/2$ and the isotropic dissipation rate is ε.

The pressure correlation term Π_{ij} can be split into a re-distribution term ϕ_{ij} and pressure diffusion $\mathcal{D}_{ij}^p$ as follows:

$$
\begin{aligned}
-\frac{1}{\rho} \left(\overline{\langle u_j' \rangle^f \frac{\partial \langle p' \rangle^f}{\partial x_i}} + \overline{\langle u_i' \rangle^f \frac{\partial \langle p' \rangle^f}{\partial x_j}} \right) = & \underbrace{\overline{\frac{\langle p' \rangle^f}{\rho} \left(\frac{\partial \langle u_j' \rangle^f}{\partial x_i} + \frac{\partial \langle u_i' \rangle^f}{\partial x_j} \right)}}_{\phi_{ij}} \\
& \underbrace{- \frac{\partial}{\partial x_m} \left(\frac{\overline{\langle u_j' \rangle^f \langle p' \rangle^f}}{\rho} \delta_{im} + \frac{\overline{\langle u_i' \rangle^f \langle p' \rangle^f}}{\rho} \delta_{jm} \right)}_{\mathcal{D}_{ij}^p}
\end{aligned}
\qquad (23)
$$

As Lumley (1978) noted, splitting the pressure correlation terms into pressure-strain and pressure diffusion terms is not unique, and the following form is also possible (Mansour et al., 1988; Craft and Launder, 1996):

$$\Pi_{ij} = \phi^*_{ij} + \underbrace{\frac{R_{ij}}{k}\frac{\mathcal{D}^p_{kk}}{2}}_{\mathcal{D}^{p*}_{ij}}, \tag{24}$$

where ϕ^*_{ij} and $\mathcal{D}^{p*}_{ij}$ are the re-defined pressure-strain and pressure-diffusion terms, respectively. Following Craft and Launder (1996); Suga (2004), $\mathcal{D}^{p*}_{kk}$ is modeled as

$$\mathcal{D}^{p*}_{kk} = \mathcal{D}^{p*}_{kk1} + \mathcal{D}^{p*}_{kk2}. \tag{25}$$

Craft and Launder (1996) provides the modeled slow part $\mathcal{D}^{p*}_{kk1}$:

$$\mathcal{D}^{p*}_{kk1} = \frac{\partial}{\partial x_k}\left\{c_{pd}(0.5d_k + 1.1d^A_k)(\nu\varepsilon k A A_2)^{1/2}\right\}, \tag{26}$$

where d_i is the inhomogeneity indicator:

$$d_i = \frac{N_i}{0.5 + (N_k N_k)^{\frac{1}{2}}}, \quad N_i = \frac{\partial \ell}{\partial x_i}. \tag{27}$$

Here, $\ell = k^{1.5}/\varepsilon$ is the turbulent length scale. The magnitude of the applied coefficient is

$$c_{pd} = 1.5(1 - A^2)[\{1 + 2\exp(-R_t/40)\}A_2 + 0.4R_t^{-1/4}\exp(-R_t/40)], \tag{28}$$

where the flatness parameter A, which converges to zero in the two-component limit (TCL), is $A = 1 - (9/8)(A_2 - A_3)$, $A_2 = a_{ij}a_{ji}$, $A_3 = a_{ij}a_{jk}a_{ki}$, and the Reynolds stress tensor is $a_{ij} = R_{ij}/k - (2/3)\delta_{ij}$. Here, $R_t = k^2/(\nu\varepsilon)$ is the turbulent Reynolds number.

Suga (2004) gave the rapid part $\mathcal{D}_{ij2}^{p*}$ as

$$\begin{aligned}\mathcal{D}_{ij2}^{p*} &= \frac{\partial}{\partial x_m}\left[\frac{\partial\langle\bar{u}_k\rangle^f}{\partial x_l}\beta_1 k\left\{\left(\ell_k\delta_{jl}-\frac{1}{4}(\ell_l\delta_{jk}+\ell_j\delta_{kl})+\frac{3}{2}\ell_k a_{jl}\right.\right.\right.\\ &\left.-\frac{3}{8}\ell_m(a_{lm}\delta_{jk}+a_{jm}\delta_{kl})\right)\delta_{im}+\left(\ell_k\delta_{il}-\frac{1}{4}(\ell_l\delta_{ik}+\ell_i\delta_{kl})+\frac{3}{2}\ell_k a_{il}\right.\\ &\left.\left.\left.-\frac{3}{8}\ell_m(a_{lm}\delta_{ik}+a_{im}\delta_{kl})\right)\delta_{jm}\right\}\right],\end{aligned} \tag{29}$$

where

$$\ell_i=\ell d_i^A,\ d_i^A=\frac{N_i^A}{0.5+(N_k^A N_k^A)^{0.5}},\ N_i^A=\frac{\partial\left(A^{0.5}\ell\right)}{\partial x_i}, \tag{30}$$

and d_i^A is another inhomogeneity indicator of Craft and Launder (1996). The model coefficient is $\beta_1=-0.05$ as given by Suga (2004).

Following the modeling strategy described in Craft and Launder (1996, 2001), the re-distribution term ϕ_{ij}^* is split into a slow term $\phi_{ij,1}$, rapid term $\phi_{ij,2}$, force production term $\phi_{ij,3}$, and inhomogeneous correction term $\phi_{ij,1}^{inh}$ and $\phi_{ij,2}^{inh}$ as follows:

$$\phi_{ij}^*=\phi_{ij,1}+\phi_{ij,2}+\phi_{ij,3}+\phi_{ij,1}^{inh}+\phi_{ij,2}^{inh}. \tag{31}$$

For the terms $\phi_{ij,1}$ and $\phi_{ij,2}$, we adopt the cubic quasi-isotropization non-linear form with two-component limit (TCL) constraints such that the corresponding component of the re-distribution term should go to zero as the velocity fluctuations approach zero along a particular direction. As in Craft and Launder (1996), the resulting forms of $\phi_{ij,1}$ and $\phi_{ij,2}$ are

$$
\begin{aligned}
\phi_{ij,1} \quad &= \quad -c_1\tilde{\varepsilon}\left\{a_{ij} + c_1'\left(a_{ik}a_{jk} - \frac{1}{3}A_2\delta_{ij}\right)\right\} - c_1''\tilde{\varepsilon}a_{ij}, && (32)\\
\phi_{ij,2} \quad &= \quad -0.6\left(P_{ij} - \frac{1}{3}P_{kk}\delta_{ij}\right) + 0.3a_{ij}P_{kk} - 0.2\left\{\frac{R_{jk}R_{il}}{k}S_{kl}\right.\\
&\quad \left. -\frac{R_{kl}}{k^A}\left(R_{ik}\frac{\partial\langle\bar{u}_j\rangle^f}{\partial x_l} + R_{jk}\frac{\partial\langle\bar{u}_i\rangle^f}{\partial x_l}\right)\right\}\\
&\quad -c_2\left\{A_2\left(P_{ij} - D_{ij}\right) + 3a_{mi}a_{nj}\left(P_{mn} - D_{mn}\right)\right\}\\
&\quad +c_2'\left[\left(\frac{7}{15} - \frac{A_2}{4}\right)\left(P_{ij} - \frac{1}{3}\delta_{ij}P_{kk}\right) + 0.1\left\{a_{ij} - \frac{1}{2}\left(a_{ik}a_{kj} - \frac{1}{3}\delta_{ij}A_2\right)\right\}P_{kk}\right.\\
&\quad -0.05a_{ij}a_{kl}P_{kl} + 0.1\left\{\left(\frac{R_{im}}{k}P_{jm} + \frac{R_{jm}}{k}P_{im}\right) - \frac{2}{3}\delta_{ij}\frac{R_{lm}}{k}P_{lm}\right\}\\
&\quad \left. +0.1\left(\frac{R_{jk}R_{il}}{k^2} - \frac{1}{3}\delta_{ij}\frac{R_{lm}R_{km}}{k^2}\right)\left(6D_{kl} + 13kS_{kl}\right) + 0.2\left(D_{kl} - P_{kl}\right)\frac{R_{jk}R_{il}}{k^2}\right], && (33)
\end{aligned}
$$

where $S_{ij} = \frac{\partial\langle\bar{u}_j\rangle^f}{\partial x_i} + \frac{\partial\langle\bar{u}_i\rangle^f}{\partial x_j}$ and $D_{ij} = -\left(R_{ik}\frac{\partial\langle\bar{u}_k\rangle^f}{\partial x_j} + R_{jk}\frac{\partial\langle\bar{u}_k\rangle^f}{\partial x_i}\right)$. The isotropic dissipation rate that approaches zero at a wall and is defined as

$$\tilde{\varepsilon} = \varepsilon - 2\nu\frac{\partial\sqrt{k}}{\partial x_k}\frac{\partial\sqrt{k}}{\partial x_k}. \qquad (34)$$

Although the wall-reflection model is usually used for the basic SMC model (Gibson and Launder, 1978), the present TCL model applies correction terms for inhomogeneity effects ($\phi_{ij,1}^{inh}$ and $\phi_{ij,2}^{inh}$) in place of the traditional wall reflection term. Those terms are basically modeled using gradients of the turbulent length scales and do not require the wall-normal distance. Following Craft

(1998), those forms are

$$
\begin{aligned}
\phi_{ij,1}^{inh} \;=\;& f_{w1}\frac{\varepsilon}{k}\left(R_{lk}d_l d_k\delta_{ij} - \frac{3}{2}R_{ik}d_j d_k - \frac{3}{2}R_{jk}d_i d_k\right) \\
&+ f_{w2}\frac{\varepsilon}{k^2}\left(R_{mn}R_{ml}d_n d_l\delta_{ij} - \frac{3}{2}R_{im}R_{ml}d_j d_l - \frac{3}{2}R_{jm}R_{ml}d_i d_l\right) \\
&+ f'_{w1}\frac{k}{\varepsilon^2}\left(R_{kl}\frac{\partial\sqrt{A}}{\partial x_l}\frac{\partial\sqrt{A}}{\partial x_k}\delta_{ij} - \frac{3}{2}R_{ik}\frac{\partial\sqrt{A}}{\partial x_k}\frac{\partial\sqrt{A}}{\partial x_j} - \frac{3}{2}R_{jk}\frac{\partial\sqrt{A}}{\partial x_k}\frac{\partial\sqrt{A}}{\partial x_i}\right),
\end{aligned} \tag{35}
$$

$$
\phi_{ij,2}^{inh} \;=\; f_I k\frac{\partial\langle\bar{u}_l\rangle^f}{\partial x_n}d_l d_n\left(d_i d_j - \frac{1}{3}d_k d_k\delta_{ij}\right), \tag{36}
$$

Following Craft (1998), the dissipation tensor ε_{ij} is modeled as

$$
\varepsilon_{ij} = (1 - f_\varepsilon)(\varepsilon'_{ij} + \varepsilon''_{ij} + \varepsilon'''_{ij})/\mathcal{D} + \frac{2}{3}\delta_{ij}f_\varepsilon\varepsilon, \tag{37}
$$

with

$$
\varepsilon'_{ij} \;=\; 2\nu\frac{\partial\sqrt{k}}{\partial x_m}\left(\frac{\partial\sqrt{k}}{\partial x_i}\frac{R_{jm}}{k} + \frac{\partial\sqrt{k}}{\partial x_j}\frac{R_{im}}{k}\right) + 2\nu\frac{\partial\sqrt{k}}{\partial x_k}\frac{\partial\sqrt{k}}{\partial x_m}\frac{R_{km}}{k}\delta_{ij} + \frac{R_{ij}}{k}\varepsilon, \tag{38}
$$

$$
\varepsilon''_{ij} \;=\; f_R\varepsilon^A\left(2\frac{R_{lk}}{k}d_l^A d_k\delta_{ij} - \frac{R_{il}}{k}d_l^A d_j^A - \frac{R_{jl}}{k}d_l^A d_i^A\right), \tag{39}
$$

$$
\varepsilon'''_{ij} = c_{\varepsilon s}\nu k\left(\frac{\partial\sqrt{A}}{\partial x_k}\frac{\partial\sqrt{A}}{\partial x_k}\delta_{ij} + 2\frac{\partial\sqrt{A}}{\partial x_j}\frac{\partial\sqrt{A}}{\partial x_i}\right), \tag{40}
$$

where $\mathcal{D} = (\varepsilon'_{kk} + \varepsilon''_{kk} + \varepsilon'''_{kk})/(2\varepsilon)$. A set of model coefficients and functions are summarized in Table 1.

The direct effects of the additional force terms (f_i and g_i^φ) on the Reynolds stress are modeled as the additional source terms F_{ij} and G_{ij}^φ in Eq.(21). However, other corresponding effects on the Reynolds stress, which need modeling, arise as a force production term $\phi_{ij,3}$ in the re-distribution term, which is mathematically expressed as

$$\phi_{ij,3} = \frac{1}{4\pi} \int_V \overline{\left(\frac{\partial (f_m + g_m^{\varphi})'}{\partial x_m} \right) \left(\frac{\partial \langle u_j \rangle^f}{\partial x_i} + \frac{\partial \langle u_i \rangle^f}{\partial x_j} \right)} \frac{dV(\boldsymbol{x'}\,)}{r} \tag{41}$$

where the integration is performed over $r = |\boldsymbol{x} - \boldsymbol{x'}|$; values with a prime superscript, herein, are the values at the position of $\boldsymbol{x'}$ while those without are values at $\boldsymbol{x}$. The simplest and widely used form for $\phi_{ij,3}$ is based on the assumption of isotropization of production (IP) as follows:

$$\phi_{ij,3} = -c_3 \left(-G_{ij} + \frac{G_{kk}}{3} \delta_{ij} \right) \tag{42}$$

where c_3 is a proportionality constant that is usually taken as $c_3 = 0.5 \sim 0.6$, and $G_{ij} = F_{ij} + G_{ij}^{\varphi}$. Another more analytical route is based on the quasi-isotropy assumption. However, this approach leads to the same form as that in Eq.(42), but with an analytically determined coefficient equal to 1/3 (Launde et al., 1975). Although the simple IP strategy has been widely used to model buoyant (Launde et al., 1975) or magnetic (Kenjereš et al., 2004) effects, we apply the TCL constraints to $\phi_{ij,3}$ as with the other re-distribution terms, rather than applying the IP model. Given the analogy of a modeling strategy for the buoyant force production with TCL constraints (Craft and Launder, 2001) (i.e., simply replacing the buoyant force term in $\phi_{ij,3}$ with the G_{ij}), $\phi_{ij,3}$ may be modeled as follows:

$$
\begin{aligned}
\phi_{ij,3} \quad = \quad & -\left(\frac{4}{10}+\frac{3}{80}A_2\right)\left(-G_{ij}+\frac{1}{3}G_{kk}\delta_{ij}\right)-\frac{1}{4}a_{ij}G_{kk} \\
& -\frac{1}{20}\left(G_{im}\frac{R_{mj}}{k}+G_{jm}\frac{R_{mi}}{k}+\delta_{ij}\frac{R_{mn}}{k}G_{mn}\right) \\
& -\frac{1}{10}\left(\frac{R_{mn}}{k}\frac{R_{mj}}{k}G_{in}+\frac{R_{mn}}{k}\frac{R_{mi}}{k}G_{jn}-\frac{1}{4}\delta_{ij}\frac{R_{mn}}{k}\frac{R_{nl}}{k}G_{lk}\right) \\
& +\frac{1}{16}\left(\frac{R_{mi}}{k}\frac{R_{nj}}{k}G_{mn}+\frac{R_{mj}}{k}\frac{R_{ni}}{k}G_{mn}+2\frac{R_{ij}}{k}\frac{R_{mn}}{k}G_{mn}\right), \qquad (43)
\end{aligned}
$$

Unlike the IP model in Eq.(42), the above form interestingly does not include any empirical coefficients to adjust (the reader is referred to Craft and Launder (2001) for a detailed derivation of $\phi_{ij,3}$). The influence of the choice of $\phi_{ij,3}$ models on the prediction results is discussed in §4.1.4

3.2. Modelling the energy dissipation rate transport equation

To complete the closure model, the transport equation for the isotropic dissipation rate is modeled as shown in Suga (2003)

$$
\begin{aligned}
\frac{\partial\tilde{\varepsilon}}{\partial t}+\langle\overline{u}_k\rangle^f\frac{\partial\tilde{\varepsilon}}{\partial x_k} = \quad & \frac{\partial}{\partial x_k}\left\{\left(\nu\delta_{kl}+0.18R_{kl}\tau\right)\frac{\partial\tilde{\varepsilon}}{\partial x_l}\right\}+c_{\varepsilon1}\frac{P_{kk}+G^{\varphi}_{kk}}{2\tau} \\
& -c_{\varepsilon2}\frac{\tilde{\varepsilon}}{\tau}-\frac{\varepsilon-\tilde{\varepsilon}}{\tau}+f_{\varepsilon3}P_{\varepsilon3}+F_{\varepsilon}, \qquad (44)
\end{aligned}
$$

where $P_k = P_{kk}/2$ is the turbulence production for the turbulent kinetic energy. Although the original paper employed elaborate forms for the model coefficient $c_{\varepsilon2}$, which was tuned after several application tests, we simply assign the model $c_{\varepsilon1} = 1.44$ and $c_{\varepsilon2} = 1.92$ as a first step for the rough wall model. The length-scale correction term in Iacovides and Raisee (1999), which corrects the energy dissipation in the vicinity of the wall and was included in the original paper, is omitted in the present study.

The production term that contains the second derivative of the mean velocity is modeled as in Jakirlić and Hanjalić (2002):

$$P_{\varepsilon 3} = -2\nu \left(\frac{\partial R_{kl}}{\partial x_l} \frac{\partial^2 \langle \overline{u_j} \rangle^f}{\partial x_k \partial x_l} + c_{\varepsilon 3} \frac{k}{\varepsilon} \frac{\partial R_{kl}}{\partial x_j} \frac{\partial \langle \overline{u_i} \rangle^f}{\partial x_k} \frac{\partial^2 \langle \overline{u_i} \rangle^f}{\partial x_j \partial x_l} \right) \tag{45}$$

A preliminary a priori test for the energy dissipation equation (results are not shown here) confirms that the modeled form of $P_{\varepsilon 3}$ yields an excessive value inside the rough wall relative to the value computed from DNS, especially for surfaces with densely distributed roughness elements. Accordingly, $f_{\varepsilon 3} = \varphi^2 \left\{ 1 - exp \left(- \left(\frac{Rt}{30} \right)^2 \right) \right\}$ is multiplied by $P_{\varepsilon 3}$ in order to restrict the effects within a rough wall. However, a further modification for $P_{\varepsilon 3}$ may be required for applying to various rough surfaces or flow configurations. The effect of the inhomogeneous roughness density term is introduced by dividing the turbulence time scale, in analogy to the model for the turbulence production term. The drag force is modeled in a similar fashion as follows:

$$F_\varepsilon = -2\nu c_{f\varepsilon 1} C_1^D \tilde{\varepsilon} - c_{f\varepsilon 2} \frac{C_2^D \langle \overline{u}_k \rangle^f}{\sqrt{\langle \overline{u}_m \rangle^f \langle \overline{u}_m \rangle^f}} \left(2 \langle \overline{u}_k \rangle^f \tilde{\varepsilon} + \frac{\langle \overline{u}_j \rangle^f R_{jk}}{\tau} - c_s R_{kl} \frac{\partial k}{\partial x_l} \right), \tag{46}$$

where we introduce the two model coefficients to model the dependence on the Reynolds number, which are given as $c_{f\varepsilon 1} = 2.3\exp \left(- \left(\frac{R_t}{25} \right)^2 \right)$ and $c_{f\varepsilon 2} = 0.6$.

4. Validation results and discussions

The developed model is validated in turbulent flows over two types of rough walls. One is a surface with randomly distributed semi-spheres. Kuwata and Kawaguchi (2018b) provides DNS and PANS results for such rough surfaces; thus, we can rigorously validate the developed model. The other is a rough surface with marine paint, which we use to assess the predictive performance for higher Reynolds number turbulent flows over real rough surfaces. The CFD code used in this study is an in-house finite-volume code STREAM (Lien and Leschziner, 1994a), developed by a group at the University of Manchester. It uses the SIMPLE pressure-correction algorithm of Patankar (1980) with non-orthogonal collocated one employing Rhie and Chow (1983) interpolation and the third order MUSCL type scheme for convection terms (Lien and Leschziner, 1994b).

4.1. Flows over surfaces with randomly distributed semi-spheres

The first model validation considers turbulent open channel flows over surfaces with randomly distributed semi-spheres. Simulation results from the presently developed model (DANS) are compared with results from the DNS and PANS simulations of Kuwata and Kawaguchi (2018a). Schematic figures for DANS, PANS, and DNS are presented in Fig.2. The DANS model does not directly solve either turbulence or the rough wall geometry, as illustrated in Fig.2(a). The PANS in Fig.2(c) does not resolve the rough wall geometry as is the case with the DANS but it does directly resolve turbulent eddy motion, whereas the DNS in Fig.2(b) directly resolves full details of the rough wall geometry and turbulence. The aim of the present study is to correctly predict the rough wall turbulence; therefore, the comparison with the DNS results is comprehensible. However, it should be remarked that the validity of the present DANS model should be evaluated through the comparison with the PANS results because the start of the present DANS model is the PANS equation without dispersive stress and with the drag force model. In other words, even if the unknown terms in the DANS equation are perfectly modeled, the simulated results do not accord with the DNS results, but rather with the PANS results.

We consider three rough surfaces (cases I, II, and III in Fig.3) with different root-mean-square roughness h_{rms} and skewness Sk values. The rough surfaces geometries are the same as those used in the DNS and PANS simulations in Kuwata and Kawaguchi (2018c,a). The statistical moment of h_{rms} measures the standard deviation of the rough surface elevation, whereas Sk characterizes whether the surface is valley-dominated or peak-dominated, which are defined as follows:

$$\begin{aligned} h_{rms}^2 &= \frac{1}{L_x L_z} \int_z \int_x (h - h_m)^2 \, dx dz, && (47) \\ Sk &= \frac{1}{h_{rms}^3 L_x L_z} \int_z \int_x (h - h_m)^3 \, dx dz, && (48) \end{aligned}$$

where L_x and L_z are the streamwise and spanwise lengths for the reference plane, respectively, and h and h_m are the surface height and mean surface height, respectively. Those statistical moments do not contain information regarding the rough surface slope. Accordingly, the effective slope (ES) of the roughness corrugation is introduced as follows (Napoli et al., 2008):

$$ES = \frac{1}{L_x} \int \left| \frac{\partial h}{\partial x} \right| dx. \quad (49)$$

Those roughness parameters (h_{rms}, Sk, and ES) for cases I, II, and III are detailed in Table 2. It is confirmed from the table that h_{rms} and Sk increase as the case number increases from I to III. This indicates that, as the case number increases, the amplitude of the rough surface elevation increases and the rough surfaces change to peak-dominated structures, which can be seen in Fig.3. In contrast to the statistical moments, the value of ES does not significantly vary (the values are in the range $ES \simeq 0.23-0.28$) among these cases. Those roughness parameters suggest that the presently tested rough surfaces have significant differences in the roughness amplitude and the peak distribution, while the slope of the undulations remains nearly unchanged.

The geometric roughness parameters required by the present model are the plane porosity φ and plane hydraulic diameter D_m, which are both given as functions of the wall-normal coordinate because the REP is considered as the plane parallel to the rough surface (Kuwata and Kawaguchi, 2018a). The profiles of φ and D_m are shown in Fig.4. Since φ and D_m respectively approach unity and zero as they separate from the bottom wall at $y/\delta = 0$, the additional force terms correspondingly weaken and eventually vanish outside the rough wall. As the case number increases from I to III, φ converges to unity at a slower rate, as shown in Fig.4(b). Meanwhile, the region where D_m plateaus ($0.1 < y/\delta < 0.15$ in case II and $0.1 < y/\delta < 0.2$ in case III) extends, as shown in Fig.4(a). These observations indicate a moderate change in the model coefficients for the plane-averaged drag force model below the roughness peak in case III. The presently used profiles of φ and D_m are the same as those in the PANS simulation of Kuwata and Kawaguchi (2018a). The detailed behavior of the drag force model coefficients in Eq.(6) are available in Kuwata and Kawaguchi (2018a).

Simulations are performed under constant friction Reynolds number of $Re_\tau = 300$ based on the half channel height δ and the friction velocity. Although the definition of the wall-shear stress is not unique, we adopt the same definition of the wall-shear stress used in Kuwata and Kawaguchi (2018a). The wall-shear stress τ_w in Kuwata and Kawaguchi (2018a) is given by a relation between the streamwise pressure gradient and τ_w as follows:

$$\tau_w = -\frac{1}{\rho}\frac{\partial P}{\partial x}(\delta - h_m) \tag{50}$$

where $\delta - h_m$ stands for the effective half channel height from the virtual origin at $y = h_m$ to $y = \delta$. Kuwata and Kawaguchi (2018b) proved that this procedure was comparable to a widely employed procedure wherein τ_w was computed by extrapolating the total shear stress (viscous and Reynolds shear stresses) to the virtual origin at $y = h_m$ (Busse et al., 2015; Forooghi et al., 2017, 2018b). It is beyond the scope of this paper to go into the details of the shear stress at the wall; therefore, the details are not described here. The reader is referred to Kuwata and Kawaguchi (2018b) for the validity of the determination procedure. We apply the slip boundary condition at the top wall and the non-slip condition at the most bottom wall. Periodic conditions are applied to the inlet and outlet boundaries to simulate the fully-developed flow. The non-uniform meshes have 120 nodes across the half-channel and 4 nodes along the streamwise direction. The rough wall region is covered by 70 nodes. The grid resolution near the interface region between the macro rough wall and clear fluid regions is refined such that the first grid point over the macro rough wall should be located at $y'^{+} < 1$ with y' being the normal distance from the macro rough wall. In addition, a sufficient number of grids is required inside the macro rough wall in order to accurately compute the derivative of the roughness parameters as they steeply change inside the rough wall. The grid independence test for case I confirms that the number of required grids inside the macro rough wall region decreases by 40%, producing a negligible difference on the skin friction coefficient (less than 1% difference). This indicates that we can choose a coarser grid inside the macro rough wall.

However, it is noted that we encounter numerical instability when we apply the too coarse grid to the rough wall region (reduced to 20%). Also, the adequate number of the grid points depends on the roughness geometry and we do not change the grid number when the roughness geometry changes; thus we adopt a sufficiently large number of grid points inside the rough wall.

4.1.1. Mean velocity

Figure 5 compares the superficial plane-averaged streamwise mean velocity $U = \varphi \langle \overline{u} \rangle^f$ normalized by the friction velocity together with the DNS data for a smooth wall from Iwamoto et al. (2002). The position of the roughness peak is also indicated using a thin line. The streamwise mean velocity within the rough wall is significantly damped due to the presence of the rough wall. One can see in the enlarged profiles in Fig.6 that the damping of U^+ is abrupt in case I, while the damping tends to be relaxed as the case number increases from I to III. This is the result of the moderate change in the roughness parameters φ and D_m near the roughness peak in case III, as shown in Fig.4. Figure 6 shows that those behaviors are quite well captured by the present DANS model. Fig.5 shows that the streamwise mean velocity in the rough wall cases substantially shifts downward compared to a smooth wall, which is due to an increase in the skin friction coefficient at the rough wall. The downward shift of U^+ is more pronounced as the case number increases, and the results in Fig.5 confirm that the DANS model closely reproduces the DNS and PANS results.

The most important required capability for a rough wall turbulence model is accurately predicting a skin friction coefficient. Accordingly, to evaluate the DANS model, the predicted skin friction coefficient C_f and the roughness function ΔU^+ are compared in Table 3. As reported by Kuwata and Kawaguchi (2018c,a), ΔU^+ by the DNS ranged from $3.5 \sim 6.8$, indicating that the simulated flows are considered to be in the transitionally rough regime. Generally speaking, in the fully rough regime, ΔU^+ can be reasonably estimated from the inner-scaled equivalent roughness k_s^+ by applying a well-known relation between ΔU^+ and k_s^+ (Nikuradse, 1933). On the other hand, there is no general relation between ΔU^+ and k_s^+ in the transitionally rough regime (Jiménez, 2004; Flack et al., 2016), although some asymptotic curves have been proposed (Nikuradse, 1933; Colebrook et al., 1939). Thus, predicting the skin friction in this regime is not straightforward. However, interestingly, we can confirm from the table that C_f from the present DANS model is consistent with the DNS and PANS results, although the DANS model underpedicts C_f in case I (the maximum difference in C_f between the DANS and DNS results is approximately 20% in case I).

4.1.2. Reynolds stress

The superficial plane-averaged Reynolds normal stresses $\sqrt{\varphi R_{ij}}$ normalized by the friction velocity are compared in Fig.7. The Reynolds stresses are damped as they approach the rough walls. As can be seen in the DNS and PANS simulation results, the maximum peak of R_{11} decreases as the case number increases from I to III, whereas R_{22} and R_{33} are insensitive to difference in the roughness geometry. The figure confirms that the developed DANS model successfully predicts the turbulence anisotropy near the rough walls. Moreover, the developed DANS model captures the damping behavior of R_{ij} in the region $0.1 < y/\delta < 0.15$. However, when one looks inside the rough wall region $0 < y/\delta < 0.1$, one can see that the Reynolds stresses predicted by the present DANS model decay too rapidly compared with the DNS results. One may expect that the underprediction of R_{ij} is attributed to neglecting the dispersive stress. However, the PANS simulation also neglects the dispersive stress, yet it shows fairly good agreement with the DNS results. Thus, the influence of dispersive stress is considered to be marginal (see Kuwata and Kawaguchi (2018a) for detailed discussions on the influence of velocity dispersion on the turbulent transport mechanism). The other possible reason is insufficient turbulence and pressure diffusion in the DANS model. Recent DNS studies suggested that pressure and turbulence diffusion played an important role in turbulent transport within the roughness (Ikeda and Durbin, 2007; Yuan and Piomelli, 2014; Kuwata and Suga, 2016; Kuwata and Kawaguchi, 2018a). However, it is well known that modeling the triple correlation of the velocity fluctuations and the pressure-velocity correlations in the Reynolds averaged Navier–Stokes framework presents some difficulties. Indeed, although Kuwata et al. (2014); Kuwata and Suga (2015) developed a turbulence model for a porous wall based on a similar strategy (modeling the double averaged equations), they also reported that damping of the predicted Reynolds normal stresses within porous media is too rapid.

4.1.3. Energy dissipation rate

In order to assess the developed model in detail, the superficial plane-averaged energy dissipation rates ε^A in each model (non-dimensionalized by the friction velocity and kinematic viscosity) are compared in Fig.8. The definition of the plane-averaged energy dissipation rate is

$$\varepsilon^A = \varphi \left\langle \nu \overline{\frac{\partial u_i'}{\partial x_k} \frac{\partial u_i'}{\partial x_k}} \right\rangle^f . \tag{51}$$

As in Kuwata and Kawaguchi (2018a), the double averaging process splits the energy dissipation ε^A into contributions from the macro-scale velocity fluctuation and velocity dispersion. However, the PANS and DANS models neglect the dispersion-related energy dissipation because those models neglect terms related to the velocity dispersion. Nevertheless, it was demonstrated by Kuwata and Kawaguchi (2018a) that the unresolved part (dispersion-related energy dissipation) could be recovered by the drag force contribution term $F_{kk}/2$. Accordingly, $\varphi(\varepsilon + F_{kk}/2)$ for the PANS and DANS results is plotted in Fig.8 in order to compare ε^A with the DNS data. The DNS results show that the maximum peak value of ε^A decreases as the case number increases from I to III, which is successfully captured by the DANS model despite the fact that the dispersion-related energy dissipation is not directly treated. However, the DANS model shows an unphysical secondary peak just above the rough surface in case I, which does not appear in the PANS results. The unphysical secondary peak occurs outside the rough wall region where the additional terms in the double averaged equation vanish. Thus, it can be said that the presently modeled roughness terms do not cause such an unphysical peak, but the unphysical peak may originate from some terms in the base turbulence model.

4.1.4. Drag force effects

In order to evaluate the modeled terms in the double averaged Navier–Stokes equation, we discuss the budget terms appearing in the streamwise DANS equation. In addition to the Reynolds shear stress, viscous shear stress, and pressure terms, additional roughness terms appear, namely the inhomogeneous roughness density and drag force terms. However, we only focus on the Reynolds shear stress and drag force contribution terms because the other terms do not include any approximation. Following Kuwata and Kawaguchi (2018a,b), the drag force contribution term $DF(y)$ in the integrated momentum equation is expressed as follows:

$$DF(y) = -\left(\int_0^y \varphi\overline{f_x}dy - \int_0^\delta \varphi\overline{f_x}dy\right). \tag{52}$$

since the term $\overline{f_x}$ is modeled as shown in Eq.(14) by applying the binomial expansion to the quadratic term with respect to the fluid velocity, we can decompose $DF(y)$ into the mean velocity contributor $DF_m(y)$ and the fluctuation velocity contributor $DF_t(y)$ as $DF(y) = DF_m(y) + DF_t(y)$:

$$\begin{aligned} DF_m(y) &= -\left(\int_0^y \varphi f_x^m dy - \int_0^\delta \varphi f_x^m dy\right). \\ DF_t(y) &= -\left(\int_0^y \varphi f_x^t dy - \int_0^\delta \varphi f_x^t dy\right). \end{aligned} \tag{53}$$

where f_x^m (first and second terms on the right hand side of Eq.(14)) and f_x^t (third term on the right hand side of Eq.(14)) in the present flow system can be reduced as follows:

$$\begin{aligned} f_x^m &= -\nu C_1^D \langle\overline{u}\rangle^f - C_2^D \left(\langle\overline{u}\rangle^f\right)^2 \\ f_x^t &= -C_2^D R_{11}, \end{aligned} \tag{54}$$

Figures 9 and 10 respectively compare $DF(y)$ and $-\varphi R_{12}$, which are both normalized by the friction velocity. The drag force contribution $DF(y)$ and its mean $DF_m(y)$ from the DANS results are plotted in Fig.9, and the total stress profiles are also included in fig.9. As shown in Figures 9 and 10, momentum transfer is dominated by Reynolds stress far from the rough walls, whereas inside the rough wall the Reynolds stress is damped by the wall-roughness and $DF(y)$ is generated instead. The DNS results show that the Reynolds stress is damped and $DF(y)$ increases at a slower rate as the case number increases from I to III. Although the Reynolds stress in case III is slightly overpredicted near $y/\delta = 0.2$ compared with the DNS and PANS results, the predicted results are generally consistent with the DNS and PANS results. Figure 9 shows that the mean velocity contribution $DF_m(y)$ dominates, meanwhile, the turbulent part $DF_t(y)$ is found to somewhat contribute especially in case III, in which the streamwise Reynolds normal stress considerably penetrates the rough wall as shown in Fig.7. We can also confirm that the drag force contribution $DF(y)$ accords quite well with the PANS results, while the mean part $DF_m(y)$ slightly underpredicts, suggesting the importance of taking turbulence for the drag force into account. Despite the marginal contribution of $DF_t(y)$ in the presently simulated cases (the contribution of $DF_t(y)$ in case III occupies 9% of $DF(y)$ at the bottom wall), it is probable that the contribution of $DF_t(y)$ is largely enhanced in higher Reynolds number flows due to increased turbulent penetration, which was also implied from the DNS study of fully-rough turbulence over modeled rough walls (Forooghi et al., 2018a).

The external forces also generate an additional force production term $\phi_{ij,3}$ in the pressure-velocity correlations. Although it is possible to model $\phi_{ij,3}$ based on the assumption of the isotropization of production, the present study chooses a more elaborate route for modeling $\phi_{ij,3}$, as in the other re-distribution terms in the TCL model. Accordingly, in order to assess the influence of the force production model on the prediction results, R_{ij} is predicted with the IP model (Eq.(42)) and compared with the present TCL model (Eq.(43)) in Fig.11. Clearly, the IP model predicts excessive damping of R_{ij}, which is particularly notable in the wall-normal component R_{22} in Fig.11(b). The wall-normal component predicted with the IP model exhibits a significant drop near $y/\delta = 0.2$, while the other components R_{11} and R_{33} still exist. Hence, the predicted turbulence reaches the two-component limit inside the rough wall, which is inconsistent with the PANS results. The primary reason is the significant sink effect provided by $\phi_{22,3}$ in the IP model. The force production in the wall-normal component in the IP model is written as follows:

$$\phi_{22,3} = -c_3 \left(-G_{22} + \frac{G_{11} + G_{22} + G_{33}}{3} \right) = -c_3 \frac{G_{11} - G_{22}}{3} - c_3 \frac{G_{33} - G_{22}}{3}. \tag{55}$$

In the present flow system, R_{22} is smaller than the other component and the drag force F_{ij} is considerably larger than G_{ij}^{φ}; thus, these correspondingly yield $G_{11} - G_{22} \simeq F_{11} - F_{22} > 0$ and $G_{33} - G_{22} \simeq F_{33} - F_{22} > 0$. This evidently leads to $\phi_{22,3} < 0$ from Eq.(55), and also suggests that the IP model evidently violates the TCL constraints because $\phi_{22,3}$ continues to act as a sink term, even though R_{22} becomes zero. In contrast to the IP model, we can find from the figure that the force production with the TCL constraints provides a more accurate prediction of the Reynolds stress within the rough wall. Therefore, one can conclude that the TCL constraints are essential to predict the damping behavior of the Reynolds stress within rough walls.

4.2. Flows over spray marine paint rough surfaces

In order to demonstrate the potential of the developed DANS model for predicting higher Reynolds number turbulent flows over complicated real rough surfaces, a second calibration is performed in turbulent channel flows over rough walls with marine paint (cases P1, P2, P3, and P4), as shown in Fig.12. The three-dimensional topographical map is measured with a 3D scanning system (Keyence VR3000) in order to obtain the geometry of the painted surfaces. The measured vertical resolution is $0.1\mu m$, and the data is digitized at an increment of 11.7 μm in the lateral directions. The sampling area is $12mm \times 9mm$ corresponding 1024×768 point data. Snapshots of the measured rough surface elevation $h - h_m$ are visualized in Fig.13. Five samples are obtained at different locations and used to calculate the roughness parameters required in the present model (φ and D_m) and the characteristic roughness values (h_{rms}, S, and ES). Table4 summarizes the characteristic roughness values for the paint surfaces. The maximum roughness height normalized by the half channel height h_{max}/δ is also included in the table. One can see that the rough surfaces have nearly the same root-mean-square height h_{rms} but a significant difference in skewness Sk and effective slope ES. Table 4 and Fig.12 show that the rough surfaces in cases P1, P2, and P3 have positive Sk, reflecting their peak-dominated structure, while the rough surface in case P4 has relatively mild negative skewness due to its valley-dominated structure. The rough surface in case P1 has sharp peaks with small wavelength while the rough surfaces in cases P2 and P3 have relatively rounded peaks. The difference in the shape of the peaks is characterized by the effective slope ES. Indeed, we find from the table that ES in case P1 is larger than those in cases P2 and P3. Although there is a variation in the ES values, the values in all samples are less than 0.20, indicating that the presently employed painted surfaces are categorized as a wavy surface rather than a rough surface (Napoli et al., 2008). We can also confirm that the roughness height occupies a relatively small fraction of the half channel height ($h_{max}/\delta = 0.0045 \sim 0.0073$), suggesting that the roughness effects are expected to be confined near the rough wall region.

Simulations are performed at the bulk mean Reynolds number of $Re_b = 5\times10^4 \sim 5\times10^6$. Periodic boundary conditions are applied in the streamwise direction, reducing the number of nodes in the streamwise direction to 4. The non-uniform mesh along the vertical direction is clustered near the rough wall. The number of nodes is 240 across the channel, which ensures the solutions are grid-independent.

4.2.1. Reynolds number dependence of roughness effects

Figure 14 shows the predicted streamwise mean velocity at $Re_b = 10^6$ with wall-scaling, together with the predicted result for a smooth wall. In Fig.14(a) U^+ in the logarithmic region $y^+ > 200$ shifts downward due to increased wall-friction at the rough surfaces. The profiles of U^+ plus the downward shift $U^+ + \Delta U^+$, shown in Fig.14(b), indicates that a slope of U^+ remains unchanged in the logarithmic region irrespective of the surface geometry. In contrast, when we focus on the damping behavior of U^+ near the rough surfaces in Fig.14(a) , we find that the damping behavior toward the rough wall strongly depends on the roughness topology. This observation is consistent with results from many other DNS and experimental studies (e.g., Schultz and Flack, 2005; Forooghi et al., 2017; Kuwata and Kawaguchi, 2018b).

To evaluate whether the DANS model can correctly reproduce the Reynolds number dependence of the roughness effects on turbulence, the skin friction coefficient C_f and downward shift value ΔU^+ are plotted against the bulk mean Reynolds number in Fig.15(a) and the inner-scaled equivalent roughness k_s^+ in Fig.15(b), respectively. Fig.15(a) also includes an empirical correlation for a smooth wall skin friction coefficient in turbulent channel flow proposed by Dean (1978). The plots in the figure correspond to $Re_b = 1.0 \times 10^5$, 5.0×10^5, 1.0×10^6, and 5×10^6. In Fig.15(b), the equivalent roughness k_s/δ for each surface is uniquely determined by fitting the computed ΔU^+ for $Re_b = 10^6$ values to the following relationship in the fully rough regime Flack and Schultz (2010):

$$B - \Delta U^+ + \frac{1}{\kappa}\ln(k_s^+) = 8.5. \tag{56}$$

where κ and B stand for the von Kármán constant and logarithmic intercept for a smooth wall, respectively; $\kappa = 0.4$ and $B = 5.0$ are chosen in the present study, following Flack and Schultz (2010). It should be stressed that k_s^+ for each Reynolds number case in Fig.15(b) is calculated based on the uniquely determined value of k_s/δ and predicted u_τ, and we do not directly compute k_s^+ (except when $Re_b = 10^6$) from Eq.(56). This means that the computed ΔU^+ and k_s^+ values (except when $Re_b = 10^6$) follows the correlation in Eq.(56), provided that the dependence of Reynolds number on the rough wall skin friction is correctly captured by the model. What can be seen immediately in Fig.15(a) that C_f in the rough wall cases shows significantly higher compared with the correlation for a smooth wall. Additionally, while C_f in Fig.15(a) shows the Reynolds number dependence in the relatively low Reynolds number region ($Re_b < 10^6$), C_f in the higher Reynolds number regions exhibits a nearly constant value, regardless of Re_b. This is consistent with the well-known observation that the friction factor is expressed as a function of the equivalent roughness (Nikuradse, 1933).

In Fig.15(b), the predicted k_s^+ is all larger than 70 wall units ($Re_b > 1.0 \times 10^5$), indicating that the simulated flows are all in the fully-rough regime, according to Nikuradse (1933). This also rationalizes the use of the correlation of Eq.(56), which is only valid in the fully-rough regime. Indeed, $k_s^+ > 800$ when $Re_b = 10^6$. Although it is true the actual range of the transitionally rough regime depends on roughness type (Flack et al., 2012), Figure 15 (b) suggests that the predicted results reasonably follow the correlation in Eq.(56), and we can conclude that the present DANS model reasonably reproduces the dependence of C_f and ΔU^+ on Reynolds number in the fully-rough regime.

4.2.2. Friction increase ratio

Finally, to evaluate the predicted value of C_f compared with other empirical methods, we compare predicted C_f values with the experimental data in Gunji et al. (2016). However, the experimental data were obtained in a Taylor-Couette (TC) flow system whose inner wall was made of the same painted rough surface used in the present study. Thus, the measured C_f value is not directly compared with that obtained in a channel flow system. However, it is beyond the scope of this paper to simulate rough-walled TC flows, and the choice of the TC flow system does not allow us to evaluate other empirical methods. Accordingly, instead of discussing C_f itself, we discuss the friction increase ratio (FIR), defined as a ratio of a rough wall skin friction coefficient C_f to that at a smooth wall C_{f0} at the corresponding Re_b

value:

$$FIR = \frac{C_f}{C_{f0}}. \tag{57}$$

This value simply measures the effect of roughness on increasing wall friction and is easily defined, even in the TC flow system. In the experiments, the Reynolds number was based on the mean centerline velocity and a gap between the inner and outer walls and was approximately 5×10^4, thus the bulk mean Reynolds number is set to $Re_b = 5 \times 10^4$ in the present simulation. For the experiments, the mean centerline velocity was used to compute C_f. For a comparison, FIR values based on other empirical methods are discussed here. One of the most promising approaches for predicting FIR in the present rough surfaces is to use the slope-based method because many DNS and experimental studies support the contention that ΔU^+ increases linearly with ES for a wavy surface when ES is less than 0.2 (Napoli et al., 2008; Schultz and Flack, 2009; De Marchis et al., 2010; Chan et al., 2015). Using the DNS data for ΔU^+ for the rough surfaces with $ES < 0.2$ in Napoli et al. (2008), we approximate the linear correlation as $\Delta U^+ = 0.2ES$. Furthermore, to compute the FIR from ΔU^+, we use the relation between ΔU^+ and a difference in the skin friction coefficients at smooth and rough walls, as proposed in Hama (1954):

$$\Delta U^+ = \sqrt{\frac{2}{C_{f0}}} - \sqrt{\frac{2}{C_f}}. \tag{58}$$

Here, the skin friction coefficient at a smooth wall C_{f0} is given as in Dean (1978):

$$C_{f0} = 0.073 Re_b^{-0.25}. \tag{59}$$

We can compute C_f from ΔU^+ using Eqs. (58) and (59), yielding FIR values from the definition of Eq.(57).

Another well-known empirical correlation for the roughness effects (quantified as k_s) is the statistical moment-based method, in which k_s is expressed as a function of h_{rms} and Sk as in Flack and Schultz (2010):

$$k_s = 4.43 h_{rms}(1 + Sk)^{1.37}. \tag{60}$$

It is also possible to determine FIR from Eq.(60) with the help of Eqs. (56) and (58), although some iterative calculations are required because FIR is not explicitly expressed in terms of k_s. One might criticize the statistical moment-based method in that it may not be a suitable choice for surfaces with lower ES values, as reported by Flack and Schultz (2010). However, we merely choose this method to compare the prediction performance provided by the present DANS model, but we do not intend to use this method to obtain precise FIR values.

Figure 16 compares the predicted FIR with measured data from Gunji et al. (2016). A line corresponding to FIRpredicted = FIRexp is also shown in Fig.16. One can clearly see from Fig.16(a) and (b) that the moment-based method overestimates FIR in all cases compared to the present DANS model. In particular, FIR is significantly overestimated in case P3. This observation is, however, not surprising because the correlation function in Flack and Schultz (2010) was originally determined for rough surfaces with higher ES values. It should be noted that k_s^+ ranges from 40 (case P4) to 99 (case P1) in the simulation at $Re_b = 5 \times 10^4$, implying that the simulated Reynolds number may not be not sufficiently high to apply the relation Eq.(56). However, the FIR value for case P3 is substantially larger than that for case P4 despite the fact k_s^+ for cases P3 and P4 take nearly the same values (40 wall units). This indicates that the overprediction for case P3 is not attributed to the use of Eq.(56), but the largely positive skewness in case P3 as seen in Table 4 causes the overprediction of FIR.

Another interesting observation from Fig.16(a) and (c) is that the DANS model results exhibit a similar trend as the results from the slope-based method. The DANS and slope-based methods both predict that the FIR is largest in case P1, and those for the other cases are relatively close. This trend is also consistent with the experimental data, although all predicted values are somewhat larger than the experimental data. The possible reason for the overprediction may come from a difference in the flow system. We assume the channel flow system when determining FIR, whereas it should be remarked that measurements were conducted in the rough-walled TC flow system whose wall-friction quantitatively differs from that in a channel flow. Nevertheless, the predicted FIR trend is reasonably consistent with the experimental data, suggesting that the present model can successfully reflect the influence of the roughness geometry on turbulence. Furthermore, the observation that the DANS and slope-based methods yield close prediction results is encouraging as this demonstrates that the present model can accurately predict an increase in the skin friction for the wavy surface as well as the well-established slope based method. However, we must emphasize that another comprehensive test is essentially required to extend the applicability of the DANS model because the presently tested rough surfaces are limited. This will be the focus of our future work.

5. Conclusions

In order to predict turbulent flows over rough surfaces without relying on the traditionally-used empirical correlation based on equivalent roughness, spatial and Reynolds-averaged equations are modeled based on the two-component limit second moment closure. The additional terms appearing in the double averaged equations are the drag force and inhomogeneous roughness density terms. The inhomogeneous roughness density terms do not require any approximation, whereas the drag force effects, which play a significantly important role in momentum and turbulence transport, are modeled in terms of the plane porosity and plane hydraulic diameter. The effects of velocity fluctuations on external drag force are modeled with the help of a binomial expansion, and the effects on the pressure-strain term are modeled with two-component limit constraints.

The developed model was first validated in turbulence over surfaces with randomly distributed semi-spheres. Although the simulated flows are in the transitionally-rough regime where the equivalent roughness-based approach cannot be easily applied, the predicted mean velocity, Reynolds stress, and energy dissipation are consistent with the direct numerical simulation data. Furthermore, two-component limit constraints are found to be essential for modeling effects of the additional forces on the pressure-strain term.

To evaluate the predictive performance for turbulent flows over real rough surfaces with higher Reynolds number, a second validation was conducted in turbulence over marine paint rough surfaces. The developed model successfully reproduces the dependence of the skin friction coefficient and roughness functions on Reynolds number in the fully-rough regime. Moreover, the results were found to qualitatively agree with the experimental data as the skin friction ratio increased.

The present study shows the great potential of the double averaged Navier-Stokes model for predicting rough wall turbulence. However, the tested surfaces in the present study are limited, and thus further calibration test is essential to extend the applicability of the DANS model for generic rough surfaces.

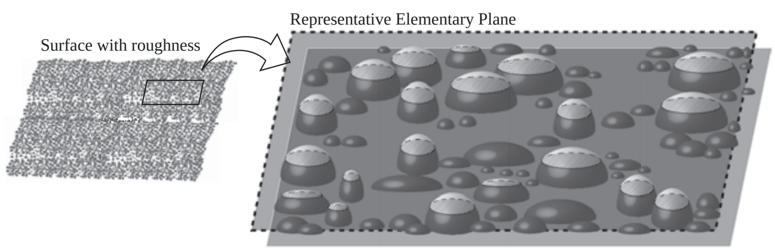

Figure 1: Schematic of a representative elementary plane.

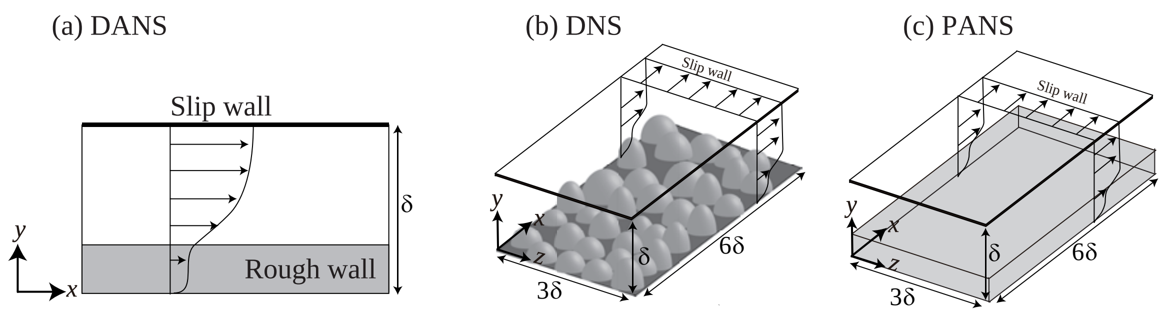

Figure 2: Computational geometry of rough-walled open channel flows: (a) double-averaged Navier-Stokes (DANS) simulation, (b) direct numerical simulation (DNS), (c) plane-averaged Navier-stokes (PANS) simulation.

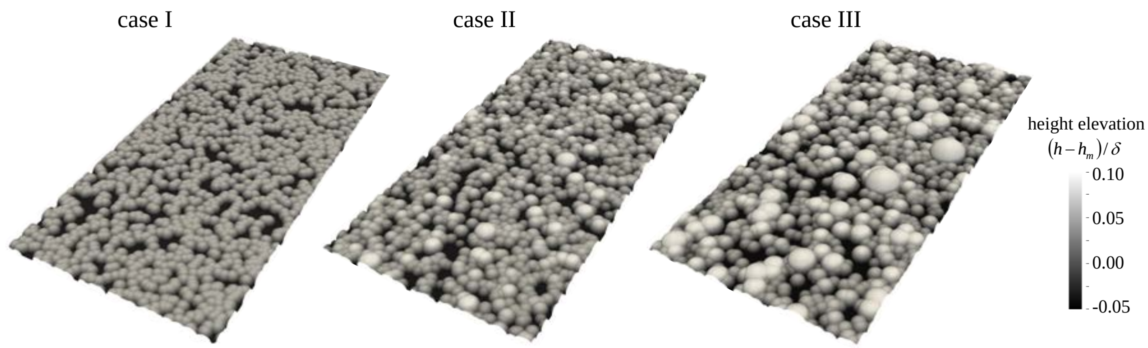

Figure 3: Surfaces with randomly distributed semi-spheres (Kuwata and Kawaguchi, 2018a) colored by their height elevation $h - h_m$: (a) case I, (b) case II, (c) case III.

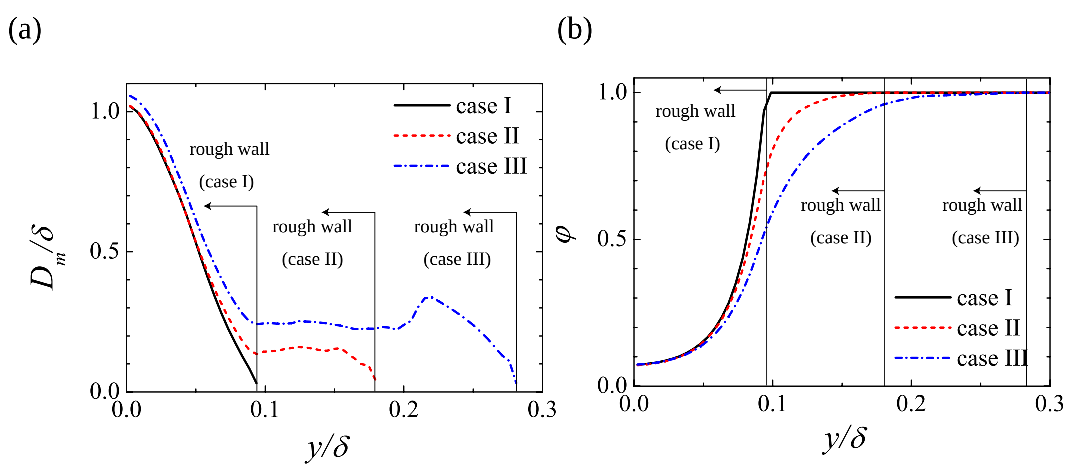

Figure 4: Profiles of characteristic rough wall parameters (Kuwata and Kawaguchi, 2018a) : (a) plane hydraulic diameter D_m, (b) plane porosity φ.

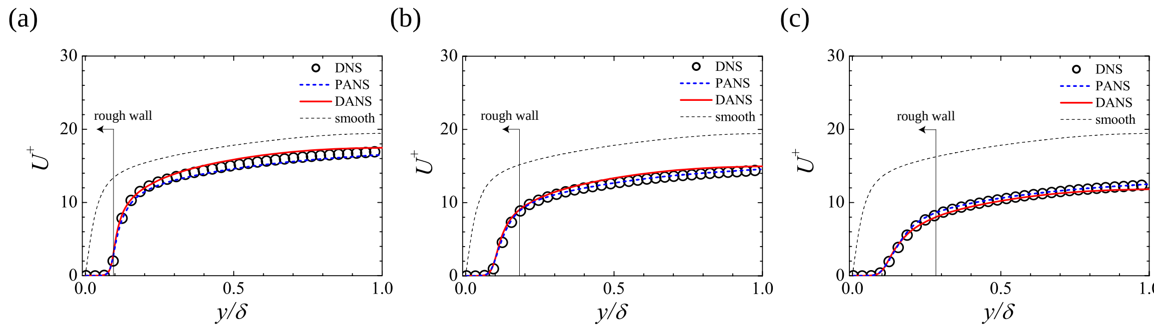

Figure 5: Comparison of the superficially plane-averaged streamwise mean velocity in the PANS and DNS results from Kuwata and Kawaguchi (2018a): (a) case I, (b) case II, (c) case III.

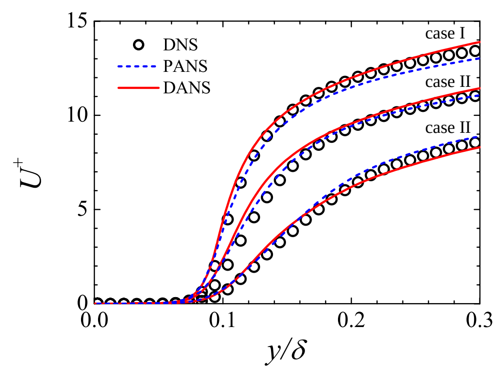

Figure 6: Comparison of the superficially plane-averaged streamwise mean velocity near rough surfaces in the PANS and DNS results from Kuwata and Kawaguchi (2018a).

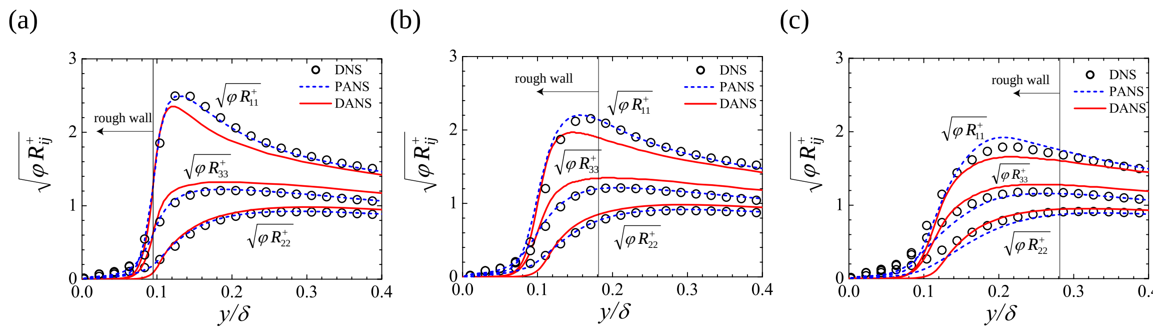

Figure 7: Comparison of the superficially plane-averaged Reynolds stresses in the PANS and DNS results from Kuwata and Kawaguchi (2018a): (a) case I, (b) case II, (c) case III.

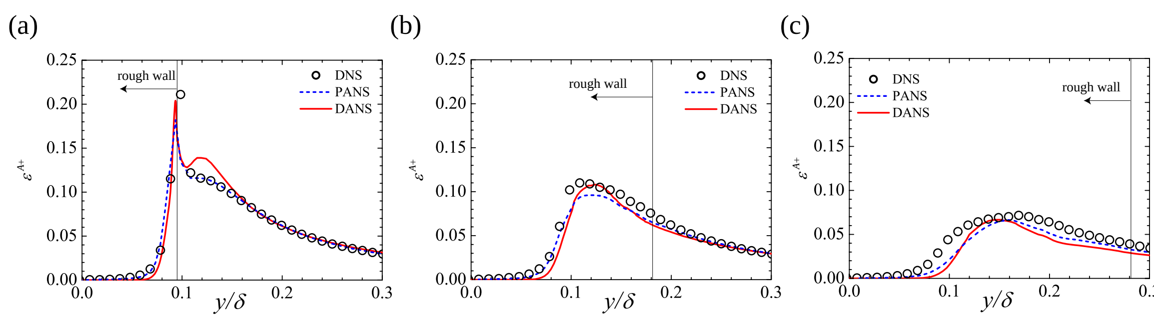

Figure 8: Comparison of the superficially plane-averaged isotropic energy dissipation rate in the PANS and DNS results from Kuwata and Kawaguchi (2018a): (a) case I, (b) case II, (c) case III.

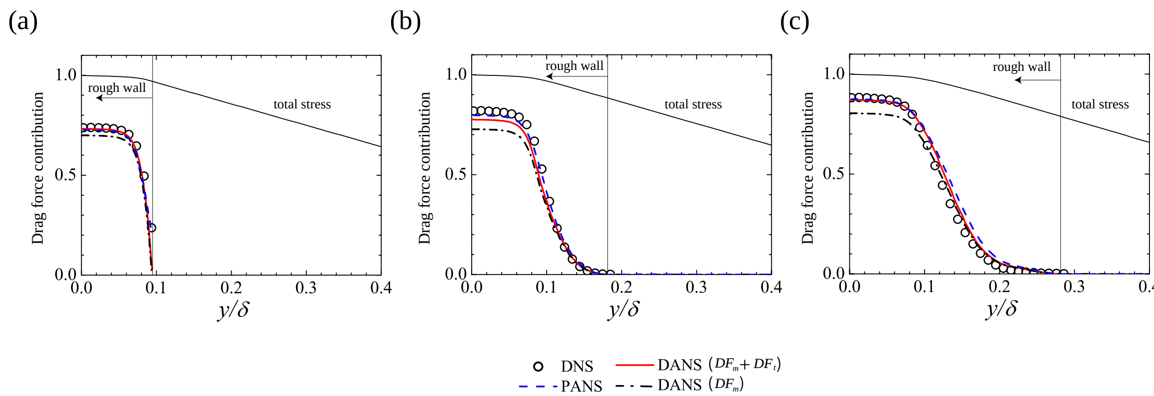

Figure 9: Comparison of the drag force contribution term $DF(y)$ in the PANS and DNS results from Kuwata and Kawaguchi (2018a): (a) case I, (b) case II, (c) case III.

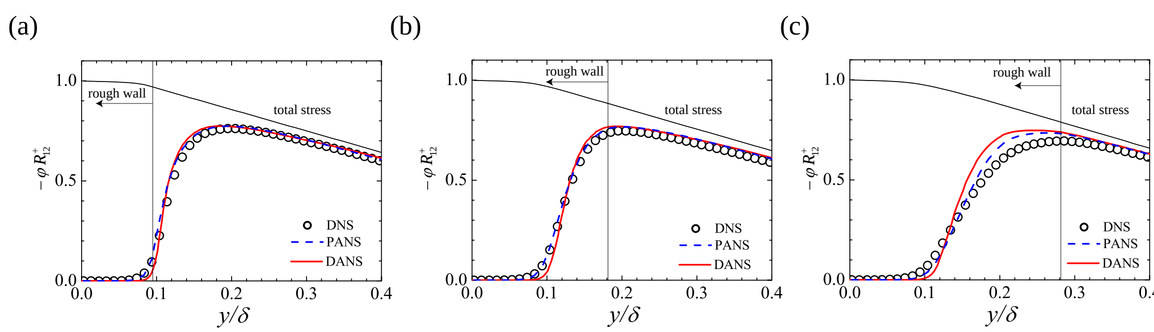

Figure 10: Comparison of the superficially plane-averaged Reynolds shear stress in the PANS and DNS results from Kuwata and Kawaguchi (2018a): (a) case I, (b) case II, (c) case III.

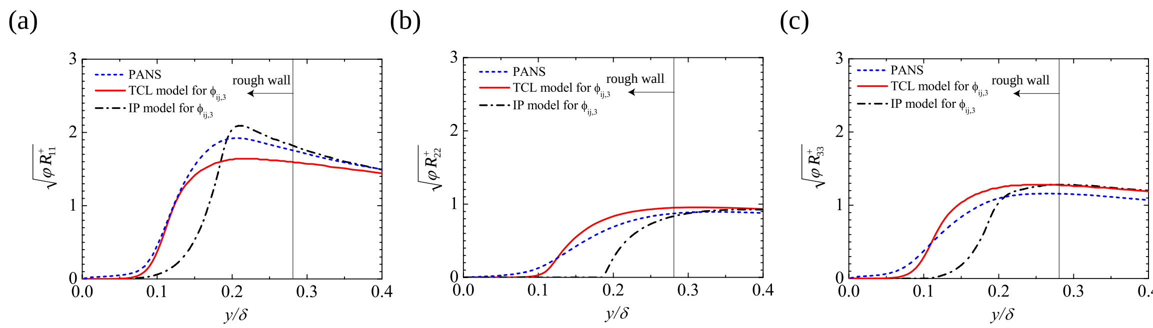

Figure 11: Superficially plane-averaged Reynolds normal stresses predicted with the IP and TCL models for the force production term in case III: (a) streamwise, (b) wall-normal, (c) spanwise components.

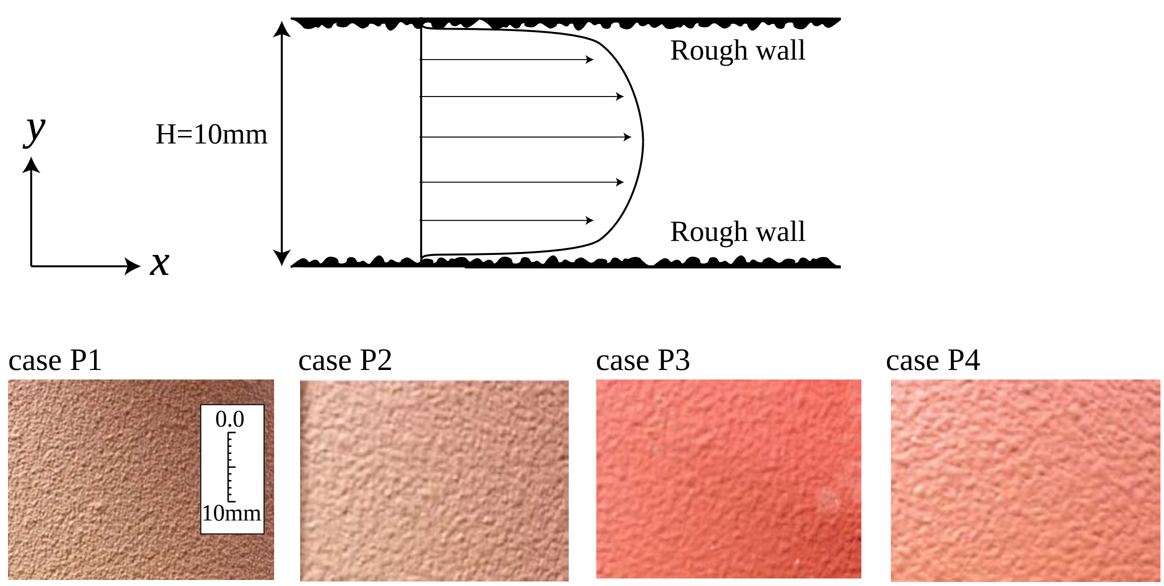

Figure 12: Computational geometry of rough-walled turbulent channel flows.

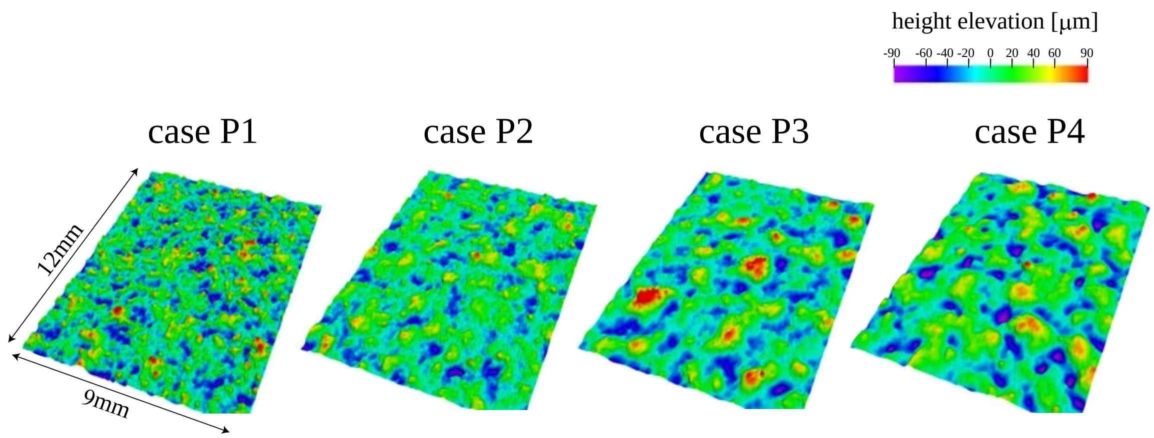

Figure 13: Snapshots of the measured rough surfaces colored by their height elevation $h - h_m$ in cases P1 to P4.

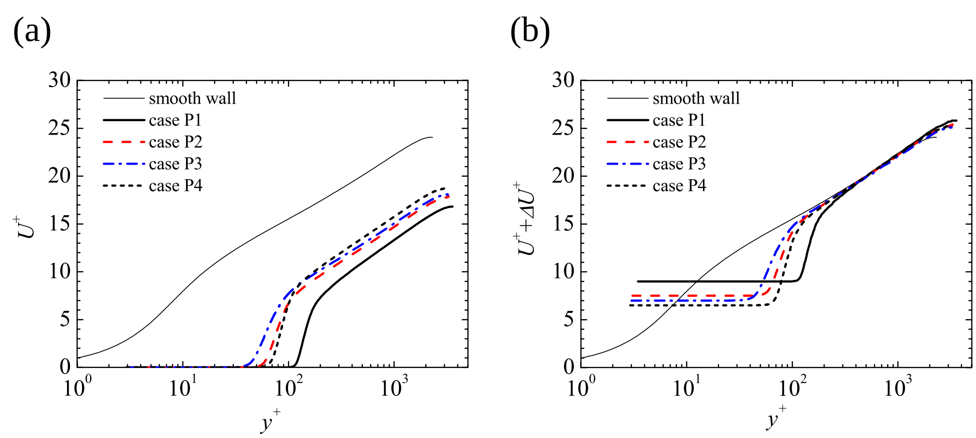

Figure 14: Streamwise mean velocity: (a) U^+ with wall-scaling, (b) $U^+ + \Delta U^+$ with wall-scaling.

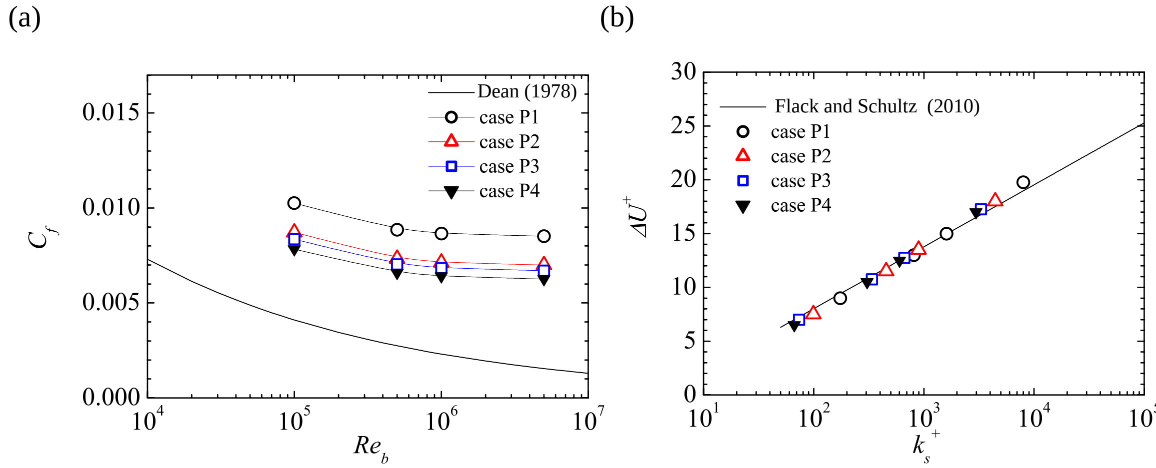

Figure 15: Dependence of the roughness effects on Reynolds number: (a) skin friction coefficient C_f together with an empirical correlation for C_f at a smooth wall from Dean (1978); (b) roughness function ΔU^+ together with a correlation function in the fully-rough regime from Flack and Schultz (2010).

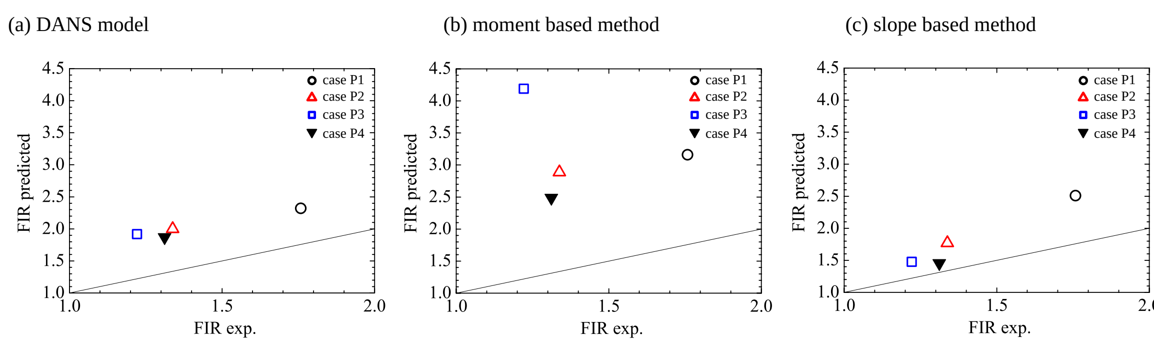

Figure 16: Comparison of the friction increase ratio (FIR) with the experimental data from Gunji et al. (2016): (a) present, (b) moment based method of Flack and Schultz (2010), (c) slope based method from Napoli et al. (2008). The solid line indicates FIR precited=FIR exp.

Table 1: Model coefficients and functions in the second moment closure model.

$f_\mu^A = \min[0.55\{1-\exp(\frac{-A^{3/2}R_t}{100})\}, \frac{3.2A}{1+S}]$	$c_1' = 1.1$	$c_2' = \min(0.6, \sqrt{A}) + f_S$	$f_{w1} = 3(1-\sqrt{A})f'_{R_t}$
$f_{w2} = 0.6A_2(1-\sqrt{A})f''_{R_t} + 0.1$	$c_1'' = A^{1/2}$	$f_{R_t} = \min\{\left(\frac{R_t}{200}\right)^2, 1\}$	
$f_A = \sqrt{A/14},\ A \leq 0.05$	$f'_{R_t} = \min\left\{1, \max\left(0, 1-\frac{R_t-55}{70}\right)\right\}$	$f'_{w1} = 0.17 + 1.3A^{2.5}$	$f''_{R_t} = \min\left\{1, \max\left(0, 1-\frac{R_t-50}{200}\right)\right\}$
$= A/\sqrt{0.7},\ 0.05 < A < 0.7$	$f_R = (1-A)\min\{(R_t/80)^2, 1\}$	$f_I = 3f_A$	$f_\varepsilon = 20A^{3/2},\ A \leq 0.05$
$= \sqrt{A},\ A \geq 0.7$	$f_S = \frac{3.5(S-\Omega)}{3+S+\Omega} - 4\sqrt{6}\min[\frac{S_{ij}S_{jk}S_{kj}}{(S_{ij}S_{ij})^{1.5}}, 0]$		$= \sqrt{A},\ A > 0.05$
$S = \tau\sqrt{(S_{ij}S_{ij})/2}$	$\Omega = \tau\sqrt{(\Omega_{ij}\Omega_{ij})/2}$		

Table 2: Characteristic parameters for surfaces with randomly distributed semi-spheres.

case	h_{rms}/δ	Sk	ES
I	0.026	-1.7	0.28
II	0.032	-0.73	0.25
III	0.047	0.21	0.28

Table 3: Comparison of the skin friction coefficient C_f and the roughness function ΔU^+ with the DNS data from Kuwata and Kawaguchi (2018a).

to Case		C_f	ΔU^+	relative difference of C_f to the DNS data
	DNS	0.0113	3.5	–
case I	PANS	0.0105	2.9	-7 %
	DANS	0.0092	2.0	-19%
	DNS	0.0145	5.1	–
case II	PANS	0.0140	4.8	-3%
	DANS	0.0131	4.6	-10%
	DNS	0.0201	6.8	–
case III	PANS	0.0201	6.8	0%
	DANS	0.0224	7.7	+11%

Table 4: Characteristic parameters for rough surfaces with marine paint.

case	h_{rms} $[\mu m]$	h_{max}/δ	Sk	ES
P1	27	0.073	0.22	0.18
P2	25	0.045	0.13	0.12
P3	27	0.045	0.68	0.084
P4	27	0.046	-0.15	0.081

Acknowledgements

The authors express their gratitude to their colleagues Dr. M. Kaneda and Dr. T.Tsukahara for their support. A part of this study was financially supported by research grants (No. 17K14591 and 16K14162) of the JSPS Japan.

References

Aupoix, B., Spalart, P., 2003. Extensions of the spalart–allmaras turbulence model to account for wall roughness. Int. J. Heat Fluid Flow 24, 454–462.

Bons, J.P., 2010. A review of surface roughness effects in gas turbines. J. turbomachinery 132, 021004.

Busse, A., Lützner, M., Sandham, N.D., 2015. Direct numerical simulation of turbulent flow over a rough surface based on a surface scan. Comput. Fluids 116, 129 – 147.

Busse, A., Sandham, N.D., 2012. Parametric forcing approach to rough-wall turbulent channel flow. J. Fluid Mech. 712, 169–202.

Chan, H.C., Huang, W.C., Leu, J.M., Lai, C.J., 2007. Macroscopic modeling of turbulent flow over a porous medium. Int. J. Heat Fluid Flow 28, 1157–1166.

Chan, L., MacDonald, M., Chung, D., Hutchins, N., Ooi, A., 2015. A systematic investigation of roughness height and wavelength in turbulent pipe flow in the transitionally rough regime. J. Fluid Mech. 771, 743–777.

Christoph, G., Pletcher, R., 1983. Prediction of rough-wall skin friction and heat transfer. AIAA Journal 21, 509–515.

Colebrook, C.F., Blench, T., Chatley, H., Essex, E., Finniecome, J., Lacey, G., Williamson, J., Macdonald, G., 1939. Correspondence turbulent flow in pipes, with particular reference to the transition region between the smooth and rough pipe laws.(include plates). J. Inst. Civil Eng. 12, 393–422.

Craft, T.J., 1998. Developments in a low-Reynolds-number second-moment closure and its application to separating and reattaching flows. Int. J. Heat Fluid Flow 19, 541–548.

Craft, T.J., Gant, S.E., Iacovides, H., Launder, B.E., 2004. A new wall function strategy for complex turbulent flows. Numerical Heat Transfer, Part B: Fundamentals 45, 301–318.

Craft, T.J., Launder, B.E., 1996. A Reynolds stress closure designed for complex geometries. Int. J. Heat Fluid Flow 17, 246–254.

Craft, T.J., Launder, B.E., 2001. Principles and performance of TCL-based second-moment closures. Flow, Turb. Combust. 66, 355–372.

Dalili, N., Edrisy, A., Carriveau, R., 2009. A review of surface engineering issues critical to wind turbine performance. Renewable and Sustainable energy reviews 13, 428–438.

Daly, B.J., Harlow, F.H., 1970. Transport equation in turbulence. Phys. Fluids 13, 2634–2649.

De Marchis, M., Napoli, E., Armenio, V., 2010. Turbulence structures over irregular rough surfaces. J. Turb. 11, 1–32.

Dean, R., 1978. Reynolds number dependence of skin friction and other bulk flow variables in two-dimensional rectangular duct flow. J. Fluids Engng. 100, 215–223.

Dirling, JR, R., 1973. A method for computing roughwall heat transfer rates on reentry nosetips, in: 8th Thermophysics Conference, p. 763.

Durbin, P., Medic, G., Seo, J., Eaton, J., Song, S., 2001. Rough wall modification of two-layer $k-\varepsilon$. J. Fluids Engng. 123, 16–21.

Dvorak, F., 1969. Calculation of turbulent boundary layers on rough surfaces in pressure gradient. AIAA journal 7, 1752–1759.

Flack, K.A., Schultz, M.P., 2010. Review of hydraulic roughness scales in the fully rough regime. J. Fluids Engng. 132, 041203.

Flack, K.A., Schultz, M.P., Barros, J.M., Kim, Y.C., 2016. Skin-friction behavior in the transitionally-rough regime. Int. J. Heat Fluid Flow 61, 21–30.

Flack, K.A., Schultz, M.P., Rose, W.B., 2012. The onset of roughness effects in the transitionally rough regime. Int. J. Heat Fluid Flow 35, 160–167.

Forooghi, P., Frohnapfel, B., Magagnato, F., Busse, A., 2018a. A modified parametric forcing approach for modelling of roughness. Int. J Heat Fluid Flow 71, 200 – 209.

Forooghi, P., Stroh, A., Magagnato, F., Jakirlić, S., Frohnapfel, B., 2017. Toward a universal roughness correlation. J. Fluids Engng. 139, 121201.

Forooghi, P., Stroh, A., Schlatter, P., Frohnapfel, B., 2018b. Direct numerical simulation of flow over dissimilar, randomly distributed roughness elements: A systematic study on the effect of surface morphology on turbulence. Phys. Rev. Fluids 3, 044605.

Getachew, D., Minkowycz, W.J., Lage, J.L., 2000. A modified form of the $k-\varepsilon$ model for turbulent flows of an incompressible fluid in porous media. Int. J. Heat Mass Transfer 43, 2909–2915.

Gibson, M.M., Launder, B.E., 1978. Ground effects on pressure fluctuations in the atmospheric boundary layers. J. Fluid Mech. 86, 491–511.

Gunji, M., Shoen, T., Mieno, H., Kawaguchi, Y., 2016. Proposal and verification of estimation method for turbulent frictional drag of irregularly roughened surface from the roughness curve measurement, in: ASME 2016 Fluids Engineering Division Summer Meeting, American Society of Mechanical Engng.. pp. V01BT25A006–V01BT25A006.

Hama, F.R., 1954. Boundary layer characteristics for smooth and rough surfaces. Trans. Soc. Nav. Arch. Marine Engrs. 62, 333–358.

Hellsten, A., 1997. Extension of the $k-\omega$-sst turbulence model for flows over rough surfaces. AIAA Journal , 1997–3577.

Iacovides, H., Raisee, M., 1999. Recent progress in the computation of flow and heat transfer in internal cooling passages of turbine blades. Int. J. Heat Fluid Flow 20, 320–328.

Ikeda, T., Durbin, P.A., 2007. Direct simulations of a rough-wall channel flow. J. Fluid Mech. 571, 235–263.

Iwamoto, K., Suzuki, Y., Kasagi, N., 2002. Database of fully developed channel flow-thtlab internal report no. ILR-0201, Rapport technique, THT-LAB, Dept. of Mech. Engng., The Univ. of Tokyo .

Jakirlić, S., Hanjalić, K., 2002. A new approach to modelling near-wall turbulence energy and stress dissipation. J. Fluid Mech. 539, 139.

Jiménez, J., 2004. Turbulent flows over rough walls. Annu. Rev. Fluid Mech. 36, 173–196.

Kenjereš, S., Hanjalić, K., Bal, D., 2004. A direct-numerical-simulation-based second-moment closure for turbulent magnetohydrodynamic flows. Phys. Fluids 16, 1229–1241.

Knopp, T., Eisfeld, B., Calvo, J., 2009. A new extension for $k--\omega$ turbulence models to account for wall roughness. Int. J. Heat Fluid Flow 30, 54–65.

Kuwata, Y., Kawaguchi, Y., 2018a. Direct numerical simulation of turbulence over resolved and modelled rough walls with irregularly distributed roughness. Int. J. Heat Fluid Flow. submitted .

Kuwata, Y., Kawaguchi, Y., 2018b. Direct numerical simulation of turbulence over systematically varied irregular rough surfaces. J. Fluid Mech. 862, pp.781–815.

Kuwata, Y., Kawaguchi, Y., 2018c. Statistical discussions on skin frictional drag of turbulence over randomly distributed semi-spheres. Int. J. Adv. Engng. Sci. Appl. Mat. , 1–10.

Kuwata, Y., Suga, K., 2015. Progress in the extension of a second-moment closure for turbulent environmental flows. Int. J. Heat Fluid Flow 51, 268–284.

Kuwata, Y., Suga, K., 2016. Transport mechanism of interface turbulence over porous and rough walls. Flow, Turb. Combust. 97, 1071–1093.

Kuwata, Y., Suga, K., Sakurai, Y., 2014. Development and application of a multi-scale $k-\varepsilon$ model for turbulent porous medium flows. Int. J. Heat Fluid Flow 49, 135–150.

Launde, s., Reece, G., Rodi, W., 1975. Progress in the development of a Reynolds-stress turbulence closure. J. Fluid Mech. 68, 537–566.

Lien, F., Leschziner, M., 1994a. A general non-orthogonal finite-volume algorithm for turbulent flow at all speeds incorporating second-moment turbulence-transport closure, Part1: Numerical implementation. Comp. Meth. Appl. Mech. Engng. 114, 123–148.

Lien, F.S., Leschziner, M.A., 1994b. Upstream monotonic interpolation for scalar transport with application in complex turbulent flows. Int. J. Num. Meth. Fluids 19, 527–548.

Ligrani, P., Moffat, R., 1986. Structure of transitionally rough and fully rough turbulent boundary layers. J. Fluid Mech. 162, 69–98.

Lumley, J.L., 1978. Computational modelling of turbulent flows. Adv. Apl. Mech. 18, 123–176.

Mansour, N.N., Kim, J., Moin, P., 1988. Reynolds-stress and dissipation-rate budgets in a turbulent channel flow. J. Fluid Mech. 194, 15–44.

Mignot, E., Barthélemy, E., Hurther, D., 2009. Double-averaging analysis and local flow characterization of near-bed turbulence in gravel-bed channel flows. J. Fluid Mech. 618, 279–303.

Miyake, Y., Tsujimoto, K., Agata, Y., 2000. A DNS of a turbulent flow in a rough-wall channel using roughness elements model. JSME Int. J. Series B Fluids Thermal Engng. 43, 233–242.

Moody, L.F., 1944. Friction factors for pipe flow. Trans. Asme 66, 671–684.

Musker, A., 1980. Universal roughness functions for naturally-occurring surfaces. Trans. Canadian Soc. Mech. Engng. 6, 1–6.

Napoli, E., Armenio, V., De Marchis, M., 2008. The effect of the slope of irregularly distributed roughness elements on turbulent wall-bounded flows. J. Fluid Mech. 613, 385–394.

Nikuradse, J., 1933. Laws of flow in rough pipes, in: VDI Forschungsheft, Citeseer.

Parent, O., Ilinca, A., 2011. Anti-icing and de-icing techniques for wind turbines: Critical review. Cold regions science and technology 65, 88–96.

Patankar, S.V., 1980. Numerical heat transfer and fluid flow. Hemisphere/ McGraw Hill, Washington.

Patel, V., Yoon, J., 1995. Application of turbulence models to separated flow over rough surfaces. J Fluids Engng. 117, 234–241.

Pedras, M.H.J., de Lemos, M.J.S., 2001. Macroscopic turbulence modeling for incompressible flow through undeformable porous media. Int. J. Heat Mass Transfer 44, 1081–1093.

Qi, M., Li, J., Chen, Q., Zhang, Q., 2018. Roughness effects on near-wall turbulence modelling for open-channel flows. J. Hydraul. Res. , 1–14.

Raupach, M.R., Shaw, R.H., 1982. Averaging procedures for flow within vegetation canopies. Boundary Layer Meteorol. 22, 79–90.

Rhie, C.M., Chow, W.L., 1983. Numerical study of the turbulent flow past an airfoil with trailing edge separation. AIAA J. 21, 1525–1532.

Schlichting, H., Gersten, K., Krause, E., Oertel, H., Mayes, K., 1960. Boundary-layer theory. volume 7. Springer.

Schultz, M.P., 2007. Effects of coating roughness and biofouling on ship resistance and powering. Biofouling 23, 331–341.

Schultz, M.P., Flack, K.A., 2005. Outer layer similarity in fully rough turbulent boundary layers. Exp. Fluids 38, 328–340.

Schultz, M.P., Flack, K.A., 2009. Turbulent boundary layers on a systematically varied rough wall. Phys. Fluids 21, 015104.

Sigal, A., Danberg, J.E., 1990. New correlation of roughness density effect on the turbulent boundary layer. AIAA journal 28, 554–556.

Silva, R.A., de Lemos, M.J.S., 2003. Turbulent flow in a channel occupied by a porous layer considering the stress jump at the interface. Int. J. Heat Mass Transfer 46, 5113–5121.

Suga, K., 2003. Predicting turbulence and heat transfer in 3-d curved ducts by near-wall second moment closures. Int. J. Heat Mass Transfer 46, 161–173.

Suga, K., 2004. Modeling the rapid part of the pressure-diffusion process in the reynolds stress transport equation. J. Fluids Engng. 126, 634–641.

Suga, K., Craft, T.J., Iacovides, H., 2006. An analytical wall-function for turbulent flows and heat transfer over rough walls. Int. J. Heat Fluid Flow 27, 852–866.

Taylor, R., Coleman, H., Hodge, B., 1985. Prediction of turbulent rough-wall skin friction using a discrete element approach. J. Fluids Engng. 107, 251–257.

Thakkar, M., Busse, A., Sandham, N.D., 2017. Surface correlations of hydrodynamic drag for transitionally rough engineering surfaces. J. Turb. 18, 138–169.

Townsin, R., 2003. The ship hull fouling penalty. Biofouling 19, 9–15.

Townsin, R., Byrne, D., Svensen, T., Milne, A., 1981. Estimating the technical and economic penalties of hull and propeller roughness. Trans. SNAME 89, 295–318.

Van Rij, J.A., Belnap, B., Ligrani, P., 2002. Analysis and experiments on three-dimensional, irregular surface roughness. ASME, Transactions, J. Fluids Engng. 124, 671–677.

Whitaker, S., 1996. The Forchheimer equation: A theoretical development. Transp. Porous Med. 25, 27–61.

Wilcox, D.C., et al., 1998. Turbulence modeling for CFD. volume 2. DCW industries La Canada, CA.

Yuan, J., Jouybari, M.A., 2018. Topographical effects of roughness on turbulence statistics in roughness sublayer. Phys. Rev. Fluids 3, 114603.

Yuan, J., Piomelli, U., 2014. Roughness effects on the reynolds stress budgets in near-wall turbulence. J. Fluid Mech. 760.